QUALITY CONTROL AND CENSUS OF SMART-R OBSERVATIONS FROM THE DYNAMO/CINDY2011 FIELD CAMPAIGN

A Thesis

by

JONATHAN MAXWELL FLIEGEL

Submitted to the Office of Graduate Studies of
Texas A&M University
in partial fulfillment of the requirements for the degree of

MASTER OF SCIENCE

Approved by:

Chair of Committee,	Courtney Schumacher
Committee Members,	Robert Korty
	Robert Washington-Allen
Department Head,	Ping Yang

December 2012

Major Subject: Atmospheric Sciences

ABSTRACT

The Shared Mobile Atmospheric Research and Teaching Radar (SMART-R) is a truck-mounted C-band, Doppler radar that was deployed during the Dynamics of the Madden-Julian Oscillation (DYNAMO) / Cooperative Indian Ocean Experiment on interseasonal variability in the year 2011 (CINDY2011) campaign on Addu Atoll, Maldives. One of SMART-R's objectives was to provide continuous volume scans of precipitating clouds during all phases of the Madden-Julian Oscillation (MJO) for the full duration of the campaign. Data from SMART-R is available for 2 October 2011 through 9 February 2012.

Every 10 minutes a full volume scan was produced, which was subsequently run through quality control algorithms that, among other filters, performed a calibration correction, noise filtering, and an attenuation correction. It was observed that data from SMART-R appeared to be slanted towards the WNW, and after analysis, a 0.75° tilt correction was applied towards azimuth 285°. The data was then converted into Cartesian coordinates and an additional noise filter was applied. NETCDF files with radial velocities and corrected reflectivity were produced.

From the reflectivity observations, a suite of products including rain maps, echo-top heights and convective/stratiform separations were produced. A modified version of the convective/stratiform separation was developed in an attempt to classify shallow and weak convection more correctly. The modified algorithm utilizes an isolation parameter set to 10 km to the north, south, east, and west, a 10-dBz echo-top height threshold set to 9 km, and a 16-dBz reflectivity threshold at 3 km to ensure only isolated, shallow, and weak rain originally classified as stratiform, is reclassified as convection.

Analyses of these products clearly suggest two MJO events occurring in October and November as indicated by the Wheeler and Hendon Multivariate MJO index. While stratiform rain almost always encompassed a larger area of the radar domain, convective rain was the larger producer of rain with the exception of active MJO periods. In addition, echo-top height counts are observed to increase in both vertical structure and frequency as the MJO initiates and becomes active over the radar domain.

Possible connections are also made between echo-top height data and humidity retrievals from soundings launched on Addu Atoll. It appears that during MJO initiation, convective echo tops lead the moistening of the mid troposphere, while during suppressed phases, the convective echo tops lag behind the moistening of the mid troposphere. Wind shear also appears to be weaker during an active MJO event, and increase as the active MJO exits the region. From these observation, as well as other rain statistics including the diurnal cycle, indicators for a localized MJO index are proposed that are based on local radar and sounding data, rather than satellite and reanalysis observations of wind and outgoing long-wave radiation.

DEDICATION

This thesis is dedicated to the people of the Maldives, specifically the residents of Addu Atoll and Hithadhoo. Thank you for your hospitality and kind nature. I fear the day that even with a magnifying glass, I will no longer be able to find your magnificent country, and the place that I called home for three months, in an atlas. I hope that day never comes.

ACKNOWLEDGEMENTS

First and foremost, I would like to thank my advisor Dr. Courtney Schumacher for both the amazing opportunity to conduct field research in paradise, and for her mentorship and guidance throughout my career at Texas A&M. I feel that I could not have chosen a better scientist to work with. I would also like to thank my other committee members Dr. Robert Korty and Dr. Robert Washington-Allen for agreeing to be on my committee and discussing my research with me.

Thanks are also due for the entire team that kept SMART-R running throughout the campaign. In addition, the support provided by the NCAR team on Addu Atoll was invaluable; most importantly of which was that of Mike Dixon who assisted greatly in the data management for SMART-R, and provided code that allowed us to adjust for the tilt in our data.

Aaron Funk provided a ton of assistance in helping me get some old C code compiled and running. If it weren't for his help, I would still probably be trying to accomplish this, with no results to show for the effort. In addition to Aaron, I would like to thank the rest of the A-Team including Justin, Ellie, Larry, Amanda, Fiaz, and Stephanie for answering all the questions I shot your way and for all of the support and encouragement you provided me.

Lastly, I would like to thank my friends and family in both Texas and Maryland. I would not have made it through these two years without all of you. I will be forever grateful for all of the friends I have made during my time in Texas and I know that our friendships will remain intact even after we go our separate ways.

TABLE OF CONTENTS

Page

ABSTRACT ii

DEDICATION iv

ACKNOWLEDGEMENTS v

TABLE OF CONTENTS vi

LIST OF FIGURES viii

LIST OF TABLES x

1. INTRODUCTION 1

2. LITERATURE REVIEW 3
   2.1 MJO Basics 3
   2.2 MJO Phase Definition 4
   2.3 Convective Spectrum of the MJO 7

3. INSTRUMENTS 11
   3.1 Radar Basics 11
   3.2 SMART-R 12
   3.3 S-PolKa 17
   3.4 Sounding Array 18

4. PROCESSING METHODOLOGY 20
   4.1 Processing Overview 20
   4.2 Raw to NETCDF 20
   4.3 NETCDF to 3DPRODUCTS 27
      4.3.1 Mask 29
      4.3.2 Rainrate 29
      4.3.3 Convective/Stratiform Separation 31
      4.3.4 Echo-top Heights 34
      4.3.5 Three-dimensional Convective/Stratiform Separation 34
      4.3.6 CS Rainrate 37

4.3.7 CS Rainrate 1 Hr 38
4.3.8 CS Rainrate 24 Hr 40

5. RESULTS 41
5.1 Introduction 41
5.2 Monthly and Full Campaign Analysis 41
5.2.1 Rainfall and Areal Coverage statistics 41
5.2.2 Echo-top Observations 47
5.3 SMART-R vs. S-PolKa 52
5.4 Rain statistics by MJO Phase 54
5.5 Diurnal Cycle 58
5.6 Humidity vs. Echo-top Heights 63
5.7 Wind Shear and Anvil 67

6. DISCUSSION 70

7. CONCLUSION 74

REFERENCES 77

APPENDIX A. MONTHLY ECHO-TOP FIGURES 83

LIST OF FIGURES

FIGURE Page

2.1 MJO phase schematic 5

2.2 MJO rain anomalies for November through March by phase in mm/hr derived from satellite data 6

2.3 Wheeler and Hendon Multivariate daily MJO index 8

3.1 SMART-R and truck on the spit site in Addu Atoll. 13

3.2 Map of Addu Atoll, Maldives and location in Indian Ocean. 14

3.3 Panoramic view from SMART-R on Addu Atoll 15

3.4 DYNAMO/CINDY2011 sounding array 19

4.1 Processing stream to convert raw polar radar data into a Cartesian NETCDF file used for analysis. 21

4.2 TRMM PR / SMART-R comparison 23

4.3 November echo-top plot w/o tilt correction 24

4.4 November echo-top plot with tilt correction 25

4.5 Three-km horizontal cross section raw to NETCDF quality control processing example from 14:36 UTC 27 Nov 2011 26

4.6 Processing stream to convert NETCDF files into 3DPRODUCTS. . . 28

4.7 DYNAMO disdrometer data with Z-R relation a=178 and b=1.44 indicated by the green line. 30

4.8 Three-km horizontal cross section product example from 14:36 UTC 27 Nov 2011 31

4.9 Convective/stratiform separation curve 33

4.10 Three-km horizontal cross section product example from 03:26 UTC 9 Nov 2011 36

5.1 SMART-R area-averaged rainfall rates 42

5.2 SMART-R percent areal coverage by rainfall type 45
5.3 10- and 40-dBz echo-top heights 48
5.4 November echo tops 50
5.5 Anvil/clutter echo tops 51
5.6 SMART-R/S-PolKa rain comparison 53
5.7 Convective/Stratiform rain by MJO phase 55
5.8 Diurnal rain cycle for stratiform (red), convective (blue), and total (black) rain as seen by SMART-R 59
5.9 Diurnal cycle of rainfall by phase 61
5.10 Humidity and 10-dBz convective echo-top heights 65
5.11 Zonal winds and 10-dBz anvil/clutter echo-top heights 68
A.1 October echo tops 83
A.2 December echo tops 84
A.3 January-February echo tops 84

LIST OF TABLES

TABLE Page

3.1 SMART-R Characteristics 14

3.2 SMART-R scan strategy 16

3.3 Planned shutdowns for SMART-R. 16

3.4 Occurrences when SMART-R stopped radiating in addition to planned shutdowns listed in Table 3.3 17

4.1 Corrupt SMART-R raw files 22

4.2 Number of NETCDF files created by UTC date 27

5.1 SMART-R rainrate statistics (mm/day) 46

5.2 SMART-R area rain statistics (%) 47

5.3 Number of days each MJO phase occurred 56

5.4 Stratiform rain percent areal coverage 57

1. INTRODUCTION

The Shared Mobile Atmospheric Research and Teaching Radar (SMART-R) is a C-band, Doppler radar and one of numerous instruments involved in the Dynamics of the Madden-Julian Oscillation (MJO) (DYNAMO) field experiment that took place October 2011 - February 2012 in the Indian Ocean. DYNAMO's purpose, along with the Atmospheric Radiation Measurement (ARM) MJO Investigation Experiment (AIME) and Cooperative Indian Ocean Experiment on interseasonal variability in the year 2011 (CINDY 2011), was to study the initiation of the MJO in the equatorial Indian Ocean, as well as the MJO's evolution farther east in the Maritime Continent.

SMART-R was stationed on Addu Atoll, Maldives and operated from 1 October 2011 - 9 February 2012. Original plans called for SMART-R to remain operational through the end of March, however, due to political upheaval in the Maldives, the project was suspended in February. Along with SMART-R, the National Center for Atmospheric Research (NCAR) deployed their S-PolKa radar on Addu Atoll from 1 October - 15 January. Radiosonde data was collected every three hours on Addu Atoll, as well as in Male, Colombo, Diego Garcia, and aboard two research vessels, the Revelle and Mirai. Both research vessels were equipped with C-band radars. The United States Department of Energy (DOE) also had two sites, one on Addu Atoll and one on Manus Island, Papua New Guinea. DOE instrumentation included, but was not limited to, vertically pointing cloud radars, radiometers, disdrometers, and precipitation gauges. The National Oceanic and Atmospheric Administration's (NOAA) P-3 aircraft and the French Falcon aircraft also participated in the campaign.

This thesis will focus primarily on data collected by SMART-R. Observations

from S-PolKa and soundings from Addu Atoll will be used to validate and provide environmental context for findings from SMART-R, but will be mentioned in only a supporting context. After a literature review of the MJO, specifications of SMART-R will be outlined, followed by a description of logistics involved in operating SMART-R, as well as the scan strategies used. Next, the procedures used for processing the radar data will be discussed, including comparisons made with the Tropical Rainfall Measuring Mission (TRMM) Precipitation Radar (PR) and correcting for an apparent tilt in the SMART-R data.

Following this, a description of algorithms to calculate rainrates, echo-top heights, and a convective/stratiform separation will be discussed; this also includes development of a modified convective/stratiform separation to better classify shallow convective rain. Results and analysis of these products will then be presented to provide a general census of convective characteristics encountered during the campaign on Addu Atoll, especially in relation to the initiation of the MJO. Potential future work will then be proposed based on conclusions and questions that arise from this data set.

2. LITERATURE REVIEW

2.1 MJO Basics

First reported by Madden and Julian (1971, 1972) as the '40-50-day oscillation', the Madden-Julian Oscillation has since become one of the major topics of research in tropical meteorology. The MJO is a large-scale area of convection that typically initiates over the western tropical Indian Ocean and propagates eastward at an average speed of 5 m/s (e.g., Knutson et al., 1986) across the Indian Ocean, through the Maritime Continent, and into the western and central Pacific Ocean (Zhang, 2005). The region surrounding the large area of convection is regarded as being in the 'active' phase of the MJO, while regions to the west and east are simultaneously in 'inactive' phases. As described by Zhang (2005), the two MJO phases are connected through overturning zonal circulations; in the lower troposphere, anomalously strong westerlies exist to the west of the convective center, where as easterlies appear to the east. Low-level convergence occurs in the active region, resulting in upper-level easterlies to the west and upper-level westerlies to the east.

The MJO also varies in strength meridionally and with season (Madden, 1986; Zhang and Dong, 2004). The primary peak season is austral summer/fall with the strongest MJO signals forming south of the equator; a secondary peak occurs during boreal summer north of the equator. Typically only one MJO event can occur at a time, although a new MJO can be forming in the western Indian Ocean while another is decaying in the central Pacific Ocean (Wheeler and Hendon, 2004). It is prudent to point out that while reported as a '40-50-day' time scale by Madden and Julian, the MJO is now recognized to occur anywhere on a 30-100-day time scale (Zhang, 2005). In addition, the MJO does not follow any semblance of a regular oscillation,

and the time interval between two MJO events is anything but consistent.

Causes for interannual variability of the MJO are tough to pinpoint. Hendon et al. (1999) show very little correlation between El-Niño Southern Oscillation (ENSO) events and MJO variability except that unusually strong warm ENSO events result in diminished MJO-related convection. Additionally, very little connection can be found between sea surface temperatures (SSTs) in any portion of the Indian or Pacific Ocean basins and MJO activity (Slingo et al., 1999). Connections with global convection and the MJO also appear to be weakly correlated (Hendon et al., 1999). MJO interannual variability appears to be internally generated, rather than based on boundary conditions produced by teleconnections. Regardless, the MJO is an important intraseasonal phenomenon with impacts across the tropics and into the mid latitudes and global models continue to struggle in simulating it, in part because its initiation mechanisms are not well understood.

2.2 MJO Phase Definition

Madden and Julian (1972) produced a schematic that has become a common basis of MJO phase definitions. Figure 2.1 shows eight phases of the MJO (F, G, H, A, B, C, D, E), each indicating the convective centers and zonal circulation as the MJO propagates east; the labels are in relation to the location of Canton Island (3S, 172W), with schematic 'A' showing convection over Canton in the Central Pacific. Since the Madden and Julian (1972) characterizations, the criteria and location of different phases has evolved to something similar to what is shown in Figure 2.2. Phases are labeled one through eight, with phase one indicating convection over east Africa and phase eight indicating convection in the western hemisphere (i.e., the east Pacific and Americas).

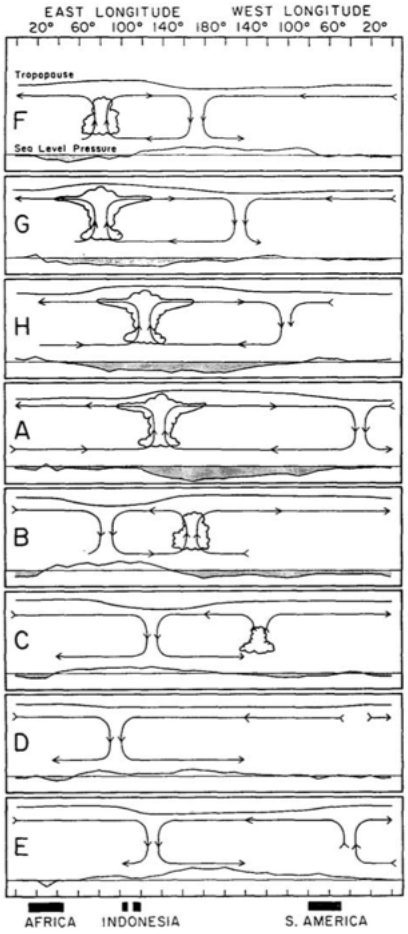

Figure 2.1: MJO phase schematic. MJO phases along the equator showing zonal circulations (indicated by arrows) and regions of convection (indicated by clouds). From Madden and Julian (1972).

In order to study the MJO and make quantitative comparisons between each phase of the MJO, an MJO index is necessary to define what phase the MJO is in at any given time. The accepted technique of doing this is through empirical orthogonal functions (EOFs), usually of outgoing longwave radiation (OLR) data, which serves as a proxy for large-scale vertical motion and deep convection. Studies including, but not limited to, Lau and Chan (1985), Knutson and Weickmann (1987), and Matthews (2000) used bandpass-filtered OLR data. Lo and Hendon (2000) improved on these indices by incorporating high-pass filtering to daily data. Wheeler and Hendon (2004)

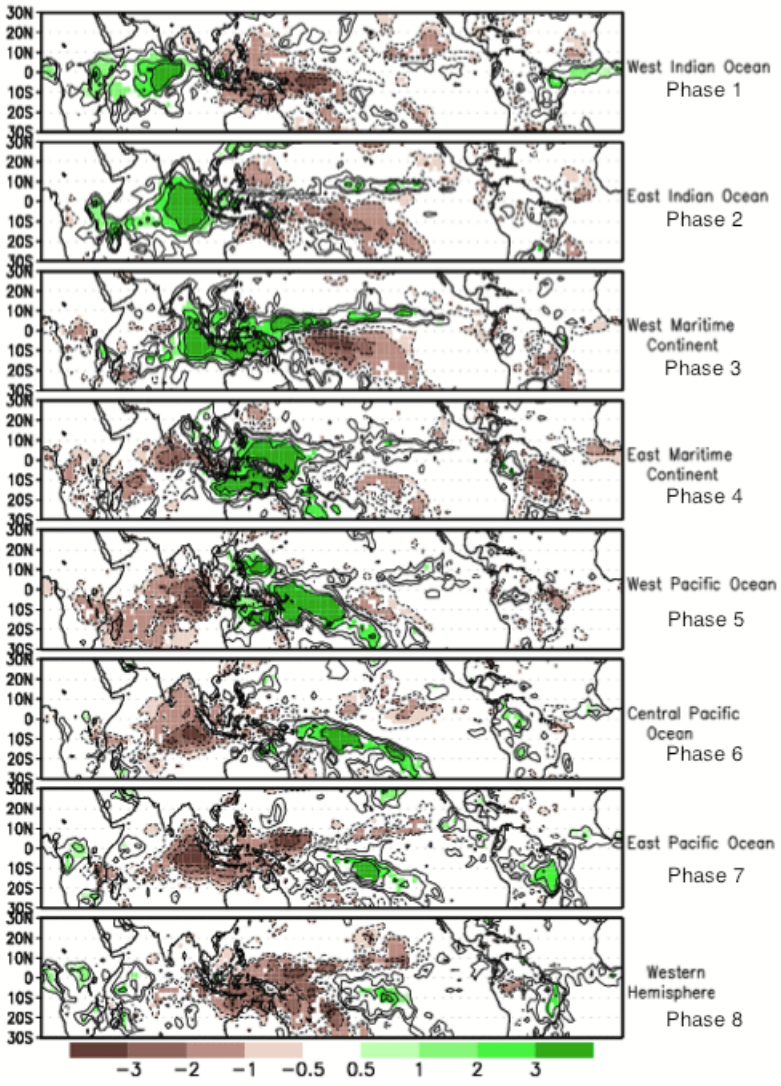

Figure 2.2: MJO rain anomalies for November through March by phase in mm/hr derived from satellite data. Plot from Gottschalck et al. (2005).

improved upon the Lo and Hendon technique by using EOFs of multiple fields instead of single field EOFs; the Wheeler and Hendon Multivariate MJO Index (Figure 2.3) will be the index used throughout this thesis.

Wheeler and Hendon (2004) found that multi-variable EOFs reduce the influence of noise from day-to-day weather. They determined that the best combination of variables for EOF representation of the MJO was OLR data, 850-hPa zonal winds,

and 200-hPa zonal winds; each variable is averaged over the domain 15°N - 15°S with 2.5° grid spacing. In order to be sure the index best quantifies MJO anomalies, the influence of the seasonal cycle is removed from each grid point by subtracting the first three harmonics of the annual cycle from the 1979-2001 period. Additional interannual trends are removed by subtracting the 120-day mean of the previous 120 days for each grid point. Furthermore, possible anomalies associated with ENSO are removed using observed SSTs. Without this filtering, strong ENSO events would falsely classify the MJO phase over the Maritime Continent and western Pacific.

Lastly, the two leading components of the EOFs are presented as the Real-time Multivariate MJO Series 1 (RMM1) and 2 (RMM2). RMM2 lags behind RMM1 by approximately 10-15 days, and their resulting values are plotted on the RMM phase space, which is divided into octants (Figure 2.3). Whichever octant the resulting RMM vector is located in determines the MJO phase for that day. Each successive day is connected with a straight line to the previous day, and the evolution of the MJO is discernable. If the absolute value of the RMM vector is less than one, the MJO is labeled as 'weak'.

2.3 Convective Spectrum of the MJO

The role and evolution of different types of cloud populations and what environment they occur in is also important to study in regards to the MJO. Until Johnson et al. (1999), shallow cumulus and deep cumulonimbus were regarded as the chief convective cloud types in the tropics. However, Johnson et al. argued that mid-level congestus clouds were also important, at least over the tropical oceans. Their work suggests that shallow and mid-level clouds generally precede the cumulonimbus, and as the moist layer deepens, the environment can support deep convection.

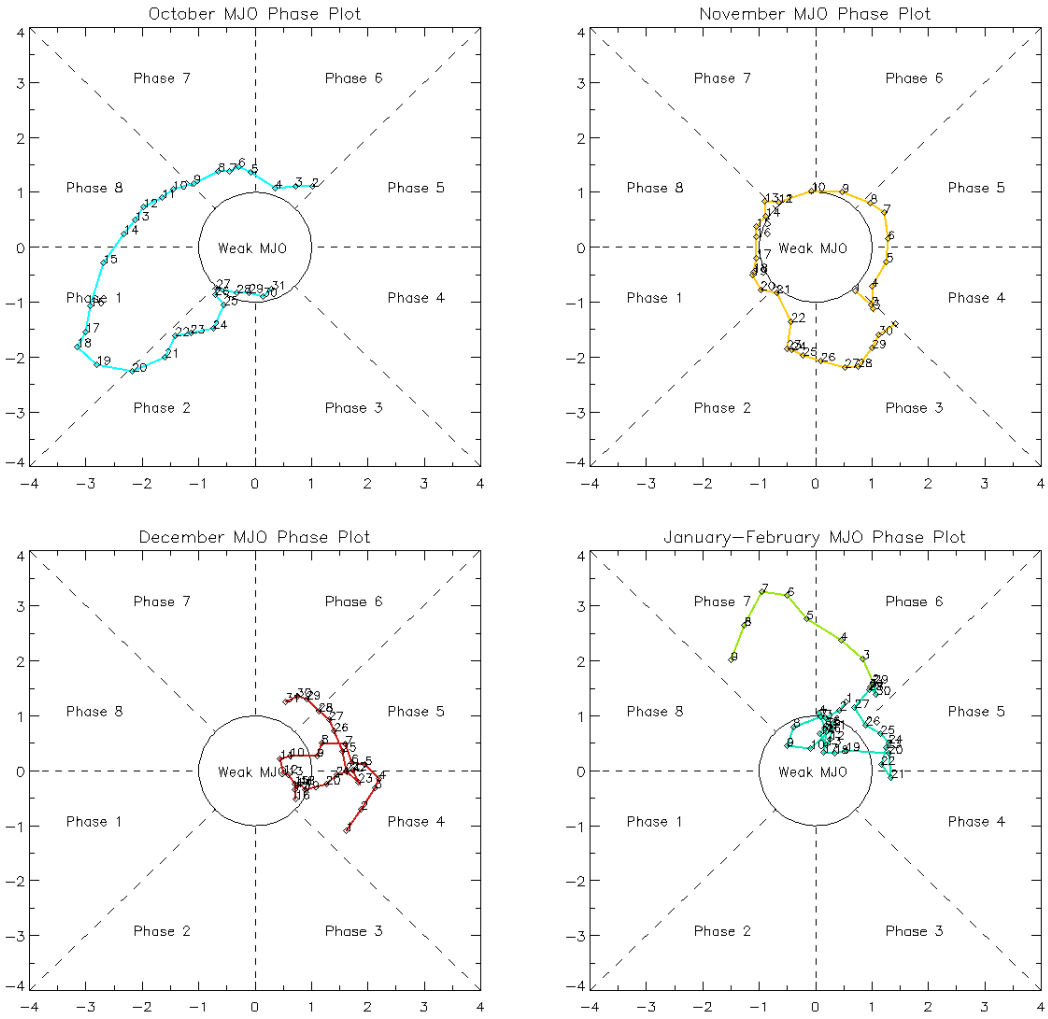

Figure 2.3: Wheeler and Hendon Multivariate daily MJO index. Index separated by month for October 2011 - February 2012. Inner circle indicates where the MJO amplitude is less than 1.0 and considered 'weak'.

Using reanalysis and radiosonde data, Kiladis et al. (2005) found similar results, showing that days prior to MJO events, low-level convergence and upward motion in the lower troposphere lead to a moistening of the boundary layer into the dry upper troposphere; the gradual buildup of shallow and mid-level convection eventually leads to deep convection. Kiladis et al. also describe that following the heaviest rain of the MJO, a westerly wind burst develops which leads to an increase in stratiform

precipitation.

Lau and Wu (2010) investigated cloud populations over the western Pacific (120°-150°E) using TRMM observations; this region is most active during MJO phase 5. They found warm rain and low clouds during phases 1 and 2, followed by a switch to mid- and upper-level mixed phase convection during the active phase buildup in phases 3 and 4. The decaying phases (6 and 7) saw an increase in the ratio of stratiform-to-convective rain. This follows the same general cloud organization described earlier of low- and mid-level convection prior to MJO initiation, which moistens the environment for development of deep convection during the active MJO, and then leads to increased stratiform rain.

The evolution of the diurnal cycle over the Indian Ocean has not been studied much in regards to overall rainfall, let alone rainfall broken down into cloud type (stratiform vs. convective) and by MJO phase. Jacobson (1976) and Gray and Jacobson (1977) looked at many ocean basins, with the tropical west Pacific most closely resembling the Indian Ocean. Using eight island stations, they observed an early morning maximum in rainfall between 0300 and 0600 local time (LT). The four larger islands also have a midday peak between roughly 1100 and 1500 LT, most likely due to a heat island influence that does not transpire on the smaller islands. All islands experience a minimum in rainfall between 1800 and 2300 LT.

Yang and Slingo (2001) investigated the diurnal cycle of rain across the tropics using satellite measurements of brightness temperature. In the Indian Ocean basin, the deepest convection was found to occur between 0200 and 0600 LT, however, the largest number of cold clouds occurs between 0600 and 1000 LT, with slightly less deep convection. This is in agreement with most oceanic observations of a diurnal cycle in precipitation, although Johnson et al. (2001) showed that in the west Pacific warm pool, a strong diurnal cycle of SSTs during suppressed phases of the MJO

can lead to more shallow convection in the late afternoon. These low- and mid-level clouds could be what precondition the environment for the deep convection experienced in active MJO phases.

Several TRMM PR studies have also been conducted that investigate diurnal rainfall patterns in the tropics. Nesbitt and Zipser (2003) looked at data from the tropics ($\pm$ 36° from the equator) and did not distinguish a strong diurnal cycle over the ocean, though they detected a late afternoon maximum over land. Sobel et al. (2011) considered the difference between diurnal rainfall over small and large islands over the maritime continent and found little evidence of a diurnal cycle over small islands, but detected one between 1000-1500 LT for larger islands. Oh et al. (2012) detected a dawn time maximum in rain over ocean regions and a late afternoon/early evening maximum over land in the western Maritime Continent.

Yoneyama et al. (2008) discusses preliminary findings from the Mirai Indian Ocean cruise for the Study of the MJO-Convection Onset (MISMO) field experiment in 2006, the first large in-situ field campaign to study the MJO in the Indian Ocean. Their findings not only reinforce the results of Johnson et al. (1999) and the role of low- and mid-level convection preconditioning the environment for deep convection, but also suggest the diurnal cycle of SSTs in the Indian Ocean also plays a role in developing low- and mid-level convection during suppressed MJO phases. Research on total precipitation by cloud type as it relates to differing phases of the MJO appears to be limited.

3. INSTRUMENTS

3.1 Radar Basics

A good description of how meteorological radars work can be found in *Radar for Meteorologists* (Rinehart, 2010). While consisting of many parts, the four main components of a radar system are the transmitter (used to generate the high-frequency electromagnetic wave the radar will use to detect objects), the antenna (used to send out the electromagnetic signal and receive it back), the receiver (used to amplify the returned signal which can sometimes be very weak), and a signal processor (used to interpret the data received and provide a meaningful unit of measurement for the data). The signal returned to the radar is some fraction of the signal originally sent out. This is expressed through the radar equation (Eq. 3.1):

$$p_r = \frac{\pi^3 p_t g^3 \theta \phi c t |K|^2 l \mathrm{z}}{1024 \ln(2) \lambda^2 r^2} \tag{3.1}$$

where p_r is the power returned, p_t is the transmitted power, l is an attenuation term, and r is the distance from the radar. The numerical constants which include π (where π = Pi), c (speed of light), 1024, ln(2), p_t, K (index of refraction, typically of liquid hydrometers) and other radar specific constants which include g (antenna gain), θ (horizontal beamwidth), ϕ (vertical beamwidth), t (pulse duration), λ (wavelength) can be grouped together as a constant C. Equation 3.1 can then be rewritten as:

$$\mathrm{z} = \frac{C p_r r^2}{l} \tag{3.2}$$

where z, the radar reflectivity factor, is a quantity that is a measure of the size distribution of the objects (hydrometeors in the case of a weather radar) detected in

a given volume. This value can be very small (for instance, fog may be around 0.001 mm^6/m^3) or rather large (e.g., 36000000 mm^6/m^3 during a large hailstorm). A more useful radar unit uses a logarithmic scale given as:

$$Z = 10 \log(\frac{z}{1\frac{mm^6}{m^3}}) \tag{3.3}$$

where Z is the logarithmic reflectivity factor and is measured in units of dBz. The logarithmic scale roughly ranges from -30 dBz for fog to +76.5 for large hail. This is the scale used to measure the intensity of meteorological targets and will be referred to as the 'reflectivity' or 'echo' seen by the radar throughout this thesis.

The value of the reflectivity indicates how intense a storm is at any given time, and with the use of a Z-R relationship (Sec. 4.3.2) can give an estimation of rainrate at a location in the radar's area of coverage. Using the reflectivity data collected by the radar and the rainrate estimations provided by the Z-R relationship, the development and progression of the MJO can be observed, and characteristics of its development and life cycle can be examined.

Finally, the most distinguishing feature of a radar is its wavelength. Radars with longer wavelengths such as S-and C-band (approximately 10 cm and 5 cm respectively) can detect large particles and do not attenuate as quickly. Shorter wavelength radars such as K_a-band (approximately 1 cm) radars are used to detect smaller cloud particles, however they attenuate much faster. This thesis will focus primarily on data collected by SMART-R, a C-band radar.

3.2 SMART-R

SMART-R is a truck-mounted C-band, Doppler radar. The radar is on a diesel International 4700 4x2 flatbed truck with an extended cab (Figure 3.1), which

houses the controls for the radar and onboard computers (Biggerstaff et al., 2005). The antenna is an 8' diameter solid parabolic reflector with shock-mounted center feed horn and radio frequency echo absorbing struts. It provides a 1.5 degree beam width and approximately 40 dB gain. The transmitter has 250kW peak power and four selectable pulse durations from 0.2 - 2.0 microseconds. It has a duty cycle of 0.001 and a selectable pulse repetition frequency (PRF) of 300 - 3000 Hz. It has horizontal polarization and a solid-state high voltage power supply and modulator. The processer is a digital SIGMET RVP-8 signal processor with selectable clutter filter, gate spacing, multiple PRF velocity dealiasing, and multiple quality control thresholds. Data collected is stored locally on a Linux hard drive until it can be transferred to other media such as a DVD or external drive. Other SMART-R specifications can be found in Table 3.1.

SMART-R was located on a spit on the lagoon side on Addu Atoll with coordi-

Figure 3.1: SMART-R and truck on the spit site in Addu Atoll.

Table 3.1: SMART-R Characteristics. From Biggerstaff et al. (2005).

Subsytem	**Description**
Transmitter	Frequency 5635 MHz
Type	Magnetron; solid-state modulator and high voltage power supply
Peak Power	250 kW
Duty cycle	0.001
Pulse duration	Four predefined values selectable from 0.2 to 2.0 μ s
Polarization	Linear Horizontal
Antenna	2.54 m diameter solid parabolic reflector
Gain	40 dB (estimated)
Half-power beam	Circular, 1.5°
Rotation rate	Selectable from 0-33 deg s^{-1}
Operational modes	Pointing, full PPI, RHI, sector scans
Signal processor	SIGMET RVP8

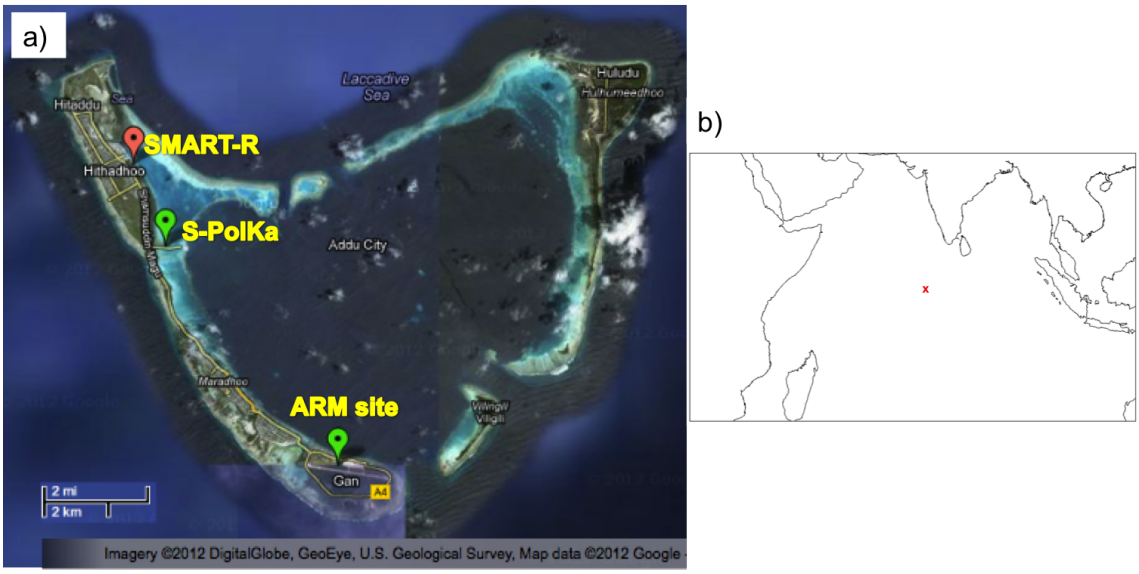

Figure 3.2: Map of Addu Atoll, Maldives and location in Indian Ocean. a) Addu Atoll, Maldives. SMART-R was located on a spit in Hithadhoo, S-PolKa was located at the wharf south of Hithadhoo, and the ARM site was located on the grounds of Gan International Airport (base map available from maps.google.com) b) Indian Ocean region with Addu Atoll marked by red 'x'.

nates 0.60752° S, 73.09575° E (Figure 3.2). The heading of the truck was 319° (0° faces due north). SMART-R did not radiate at elevation angles below 15° between

azimuth angles 302° - 336° so as not to radiate the cab of the truck. Significant low-level blockage was observed to the south and west (160° - 302°) due to a tree line approximately 0.23 km away from SMART-R, perpendicular to the shore (Figure 3.3). This blockage affected the ability to collect meaningful data at lower tilt elevation angles.

SMART-R operated on a 10-min scan cycle, starting at minute 0, 10, 20... of every hour, for six total scan cycles per hour. Three range-height indicator (RHI) scans out to 100 km directed over the DOE second ARM mobile facility (AMF2) site at Gan International Airport (Figure 3.2) were performed at the beginning of each 10-min cycle at azimuth angles 146°, 147°, and 148°, with elevation angles up to 60° (on 21 Nov 2011 at 1030 UTC, RHI scans were changed to 0°, 90°, and 147°). Following this, a surveillance scan was performed at a 0.5° elevation out to 300 km. At about two and six minutes after the beginning of each 10-min cycle, a full volume scan of 13 elevation angles was performed out to 150 km (Volumes A and B); the two scans were then interleaved together as will be described in Section 4.2. Table 3.2 specifies angles for the full volume scans and other aspects of the SMART-R scan strategy.

SMART-R was run continuously throughout the DYNAMO field campaign. However, it was shut down for routine maintenance every other week, which included an oil change. These maintenance breaks usually took SMART-R offline for roughly 40 minutes, but this varied. Table 3.3 lists planned shutdowns of SMART-R during the

Figure 3.3: Panoramic view from SMART-R on Addu Atoll. Black line indicates approximate due north. Low-level blockage can be seen towards the west.

campaign. SMART-R also had occasions when it stopped radiating; these are listed in Table 3.4. Overall, SMART-R had a collection rate of 97.8%.

Table 3.2: SMART-R scan strategy.

Scan Type	Pulse Duration (μs)	Gate Length (m)	PRF (Hz)	Nyquist Velocity (m/s)	Rotation Speed (°/s)	Max Range (km)	Elevation Angle (°)
RHI	0.6	100	1500	20	12	100	0-60
SURV	1.5	125	500	6.7	18	300	0.5
VOL	0.6	100	1000	13.3	24	150	See Below
	Volume Scan Elevation Angles						
Vol A	0.5, 1.0, 2.3, 3.6, 5.2, 7.0, 9.0, 11.2, 13.6, 16.6, 20.1, 24.4, 29.5						
Vol B	0.5, 1.6, 2.9, 4.4, 6.1, 8.0, 10.1, 12.4, 15.0, 18.3, 22.2, 26.8, 33.0						

Table 3.3: Planned shutdowns for SMART-R.

Date	Time	Missed Merged Files	Notes
2 Oct 2011	0530-0559	4	Communications Maintenance
6 Oct 2011	0440-0459	2	Drifting Clock Reset
13 Oct 2011	0410-0429	2	Drifting Clock Reset
15 Oct 2011	0540-0649	7	Oil Change
29 Oct 2011	0900-0939	4	Oil Change
12 Nov 2011	1002-1109	7	Oil Change
21 Nov 2011	1050	1	Scan Strategy Edit
26 Nov 2011	1020-1215	12	Oil Change
11 Dec 2011	0840-1006	9	Oil Change
25 Dec 2011	0800-1219	26	Oil Change / RVP8 Issue
29 Dec 2011	0612-0639	3	RVP8 Testing
8 Jan 2012	0851-0939	5	Oil Change
8 Jan 2012	1731-2359	40	Generator Issue
9 Jan 2012	0000-0939	58	Generator Issue
13 Jan 2012	0521-0739	14	Low Fuel
15 Jan 2012	0956-1030	4	Software Issue
22 Jan 2012	1051-1149	6	Oil Change
6 Feb 2012	0900-1009	7	Oil Change

Table 3.4: Occurrences when SMART-R stopped radiating in addition to the planned shutdowns listed in Table 3.3.

Date	Time	Missed Merged Files	Notes
6 Oct 2011	1700-2359	42	Continued into 7 Oct 2011
7 Oct 2011	0000-0339	22	
19 Nov 2011	0400-0439	4	
8 Dec 2011	1920-2119	12	
14 Dec 2011	1600-1829	15	
7 Jan 2012	1600-1829	16	
8 Jan 2012	0341-0719	22	
8 Jan 2012	1351-1719	21	Separate incident from above

3.3 S-PolKa

S-PolKa is an NCAR facility that contains both an S- and K_a-band radar. The S-band is dual polarimetric, meaning that it sends out alternating horizontal and vertical pulses. In addition to the more standard radar fields of radial velocity and reflectivity, a dual-polarimetric radar is able to observe a number of other fields which in turn allows for particle identification (snow, rain, graupel, etc.) and a rainrate estimate without using the standard Z-R relationship. The K_a-band is more sensitive to non-precipitating clouds and the differential attenuation compared to the S-band allows for humidity profile retrievals at low levels. However, the K_a-band attenuates very easily given its smaller wavelength and thus is limited in range and during heavy rain events.

The S-PolKa system was stationed just south of SMART-R at the wharf site (Figure 3.2) and operated from 1 October 2011 through 15 January 2012. It performed a full volume scan every 15 min consisting of eight elevation angles up through 11 degrees. During the remainder of the time, S-PolKa performed RHI sector scans in various areas in its eastern domain. For the purposes of this thesis, only the full volume scans will be examined in an attempt to better understand the potential

geographical bias SMART-R experienced due to low-level blockage; S-PolKa rainrates from the 180 degree sector SMART-R could see will be compared with the 180 degree sector SMART-R was blind to. In addition, rainrates from S-PolKa will be compared with SMART-R for the 180 degree sector SMART-R was able to collect data for.

3.4 Sounding Array

A sounding network was deployed throughout the DYNAMO campaign in the central Indian Ocean as depicted in Figure 3.4 with the exception of the Seychelles station, which never came online. Soundings refer to an instrument attached to a weather balloon that records weather observations every couple of seconds as they ascend through the atmosphere. Data collected includes pressure, temperature, wind speed, wind direction, and relative humidity. Soundings were launched up to eight times daily at six locations; Male, Colombo, Gan Island, and the Revelle made up the 'northern' sounding array, and Gan Island, the Revelle, the Mirai, and Diego Garcia made up the 'southern' array. For the purposes of this thesis, sounding data will be used from the Gan Island location to draw connections between environmental features of the atmosphere and data collected using SMART-R, such as the life cycle of echo-top heights. Sounding data from Gan Island is courtesy of DOE and the Maldivian Meteorology Service.

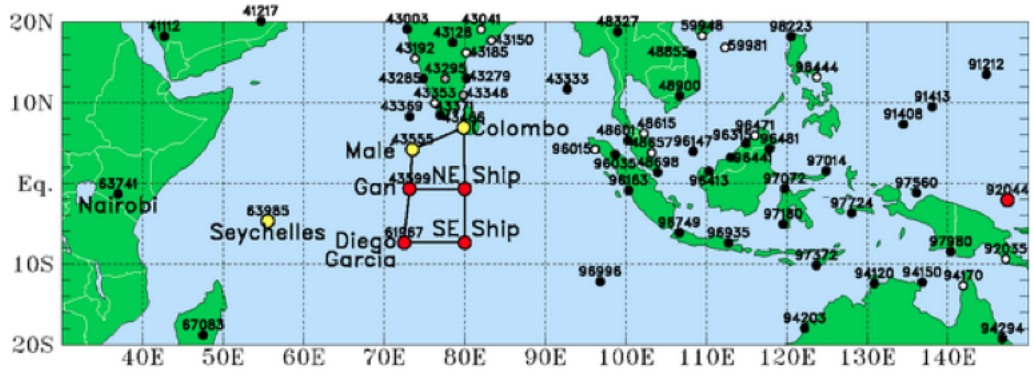

Figure 3.4: DYNAMO/CINDY2011 sounding array. Sounding station indicated by red and yellow markers. All stations shown launched eight soundings per day. Manus station shown at approximately 148°E. Seychelles station was never operational. From the DYNAMO Operations Plan.

4. PROCESSING METHODOLOGY

4.1 Processing Overview

The processing of SMART-R data can be split into two processing streams: 1) raw to interpolated NETCDF (Network Common Data Form) files and 2) rain statistics derived from the interpolated NETCDF files. As described in section 4.2, SMART-R's raw files must be run through various algorithms that calibrate the data, correct an apparent tilt in the data, and covert the data to a cartesian coordinate system, among other processing steps. Once files have reached their final NETCDF stage, they are run through algorithms that calculate rainrates, convective/stratiform separations, and echo-top heights; these are described in section 4.3

4.2 Raw to NETCDF

The processing stream to convert raw radar data into three-dimensional NETCDF files is depicted in Figure 4.1. The IRIS software used by SMART-R creates raw SIGMET files for each RHI, surveillance, and full volume scan (separate files for Volume A and Volume B). The raw files are created in polar coordinates. To process the full volume scans, the SIGMET files are first converted into Universal Format (UF) using the National Aeronautics and Space Administration's (NASA) Radar Software Library (RSL). On occasion, a UF file cannot be created due to a corrupted RAW file; instances of this are listed in Table 4.1. Then, the two 4-min UF files per 10-min scan cycle are merged; the two 13-tilt volume scans are combined to form one 26-tilt for each 10-min cycle (the 0.5° occurs in both scans). In the event that one or both UF files are not created, either because SMART-R was turned off or a corrupted RAW file was created, no UFMERGE file will be created for that time

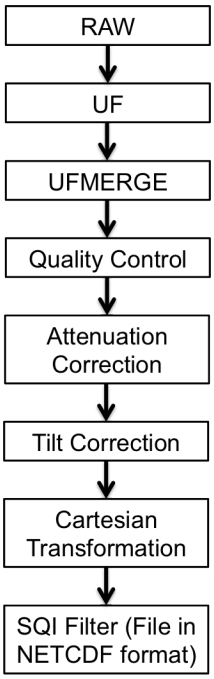

Figure 4.1: Processing stream to convert raw polar radar data into a Cartesian NETCDF file used for analysis.

period.

Once UFMERGE files are created, they are run through a quality control algorithm (Houze et al., 2004). The algorithm has Signal Quality Index (SQI) filters; SQI is a measurement of the coherence of Doppler power in the linear channel. It ranges from 0 - 1, with 0 corresponding to white noise, and 1 corresponding to a perfectly coherent Doppler target. In the present study, the filter is set to 0.2 below 4 km and 0.1 at and above 4 km to further remove noise and second-trip echo. Also included in the quality control adjustment is a calibration correction based on the methodology described in Schumacher and Houze (2000). SMART-R ran hot compared to S-PolKa, and a comparison with TRMM PR data revealed an offset of approximately 8 dB (Figure 4.2). The TRMM PR, which has a horizontal swath of 245 km and generally goes over a particular region every other day, begins to see reliable data around 18 dBz (Schumacher and Houze, 2006). The calibration thresh-

old was chosen to be 19 dBz because TRMM PR data is considerably better there and SMART-R has more data available for comparison at lower reflectivity thresholds. Comparisons were made between the swath of area TRMM PR sees during a pass over the SMART-R domain over 58 occurrences from 2 October through 23 December. Following the quality control algorithm, reflectivity data is corrected for attenuation using a routine based off of code provided by Colorado State University

Table 4.1: Corrupt SMART-R raw files. UF files could not be produced for these timestamps.

Date	Time	Missed Merged Files	Notes
2 Oct 2011	1951	1	
3 Oct 2011	0025, 0141, 0352, 1835, 2235	5	
4 Oct 2011	0301, 0515	2	
23 Oct 2011	0355, 1835	2	
26 Oct 2011	0235	1	
28 Oct 2011	0251, 1321, 2205	3	
30 Oct 2011	0301, 0331, 1615	3	
31 Oct 2011	0301	1	
1 Nov 2011	0135, 0231, 0335, 0941, 1001, 1015, 1021, 1045, 1051, 1055, 1151, 1201, 1205, 1221, 1231, 1251, 1255, 2150	15	18 total 'bad' UF files but some occurred in same 10-min period resulting in only 15 Missed Merged Files
2 Nov 2011	1815, 2245	2	
3 Nov 2011	0111, 0251, 1131	3	
7 Nov 2011	1841, 2041	2	
8 Nov 2011	0111, 0335, 0451, 1556	4	
9 Nov 2011	1735	1	
10 Nov 2011	1231, 1241, 1251	3	
16 Dec 2011	0521	1	
22 Dec 2011	0701	1	
26 Dec 2011	0431	1	
3 Feb 2012	1425	1	
4 Feb 2012	1341	1	
7 Feb 2012	0001, 1255, 1355	3	

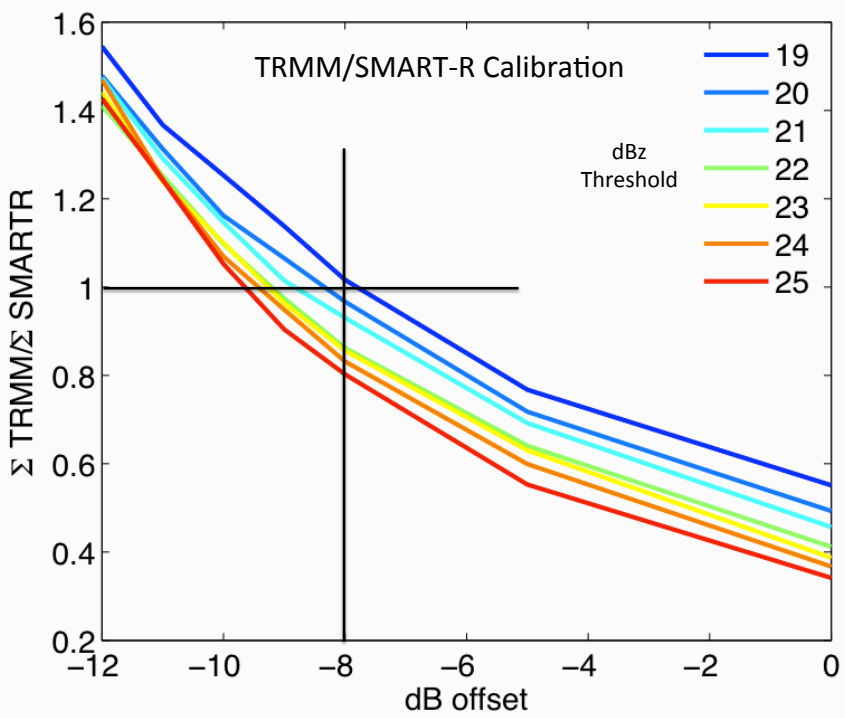

Figure 4.2: TRMM PR / SMART-R comparison. Comparison of TRMM PR and SMART-R data reveals approximately an 8 dB offset. The lowest threshold visible to TRMM PR is ∼19 dBz. Since there is more SMART-R data available at 19 dBz, this was the value chosen for calibration.

(CSU). This code corrects artificially low reflectivity values that result from power loss after the beam goes through a region of strong rain.

It became clear during preliminary processing runs of the data that SMART-R had an apparent tilt. Figure 4.3 shows the average November echo-top height map, which indicates higher tops within the non-blocked regions towards the northwest and lower values towards the southeast. This result is not expected over the course of a month, as echo-top heights should be relatively symmetric at any given radius from the radar. Some gradient is expected due to beam spreading, however, this should be similar in any azimuthal direction. The most likely culprit of the tilt is

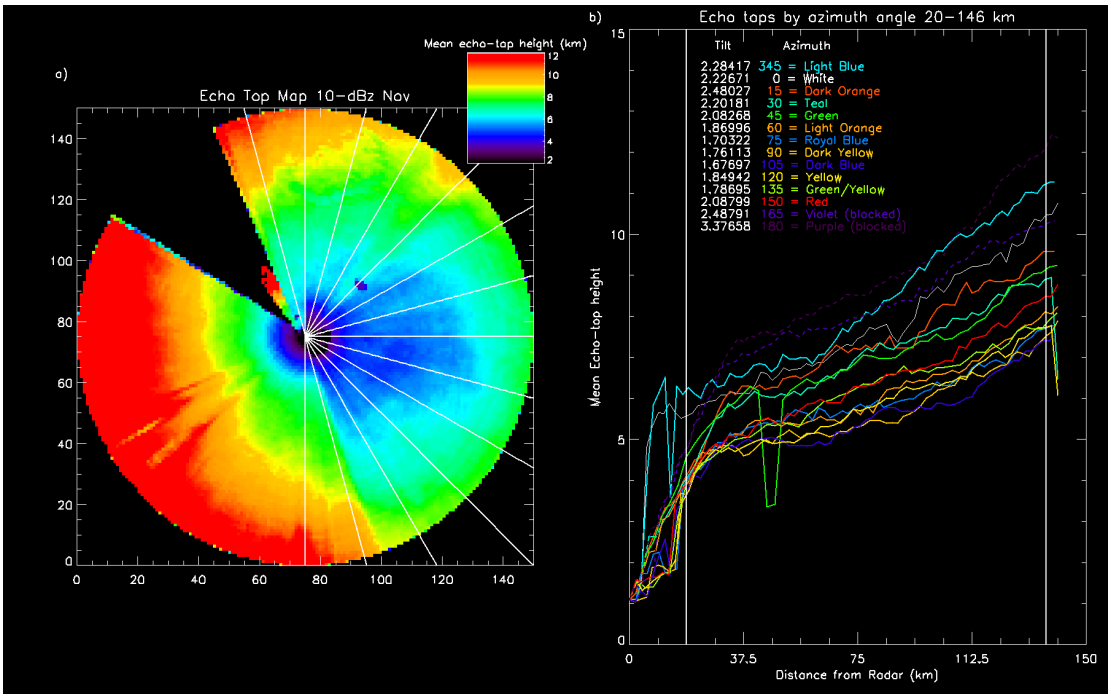

Figure 4.3: November echo-top plot w/o tilt correction. a) November 10-dBz averaged echo-top map with no tilt correction. b) Lines indicate tilt along varying azimuths as indicated by color. Each line corresponds to a white line in a). Values indicated on figure correspond to tilt angle from 20 km out to 146 km.

the truck settling on the sand and coral spit. Given the direction of the tilt, it was most likely the front left tire that sank.

Following the attenuation correction, the apparent tilt is corrected for by using a version of NCAR's Radx software developed by Mike Dixon. It employs user-defined inputs for the direction and the degree of the tilt and corrects the data in a similar way that aircraft radar data is corrected using pitch and roll information. A value of 285° was selected as the direction of the tilt. This was based on Figure 4.3 and plots of other months that indicate the lowest echo tops to generally be in the 105° direction. Tuning of the degree of tilt resulted in an average value of roughly 0.75°. While it appears the degree of tilt increased from October through February, it was not a significant change and thus a constant correction was selected. Figure 4.4

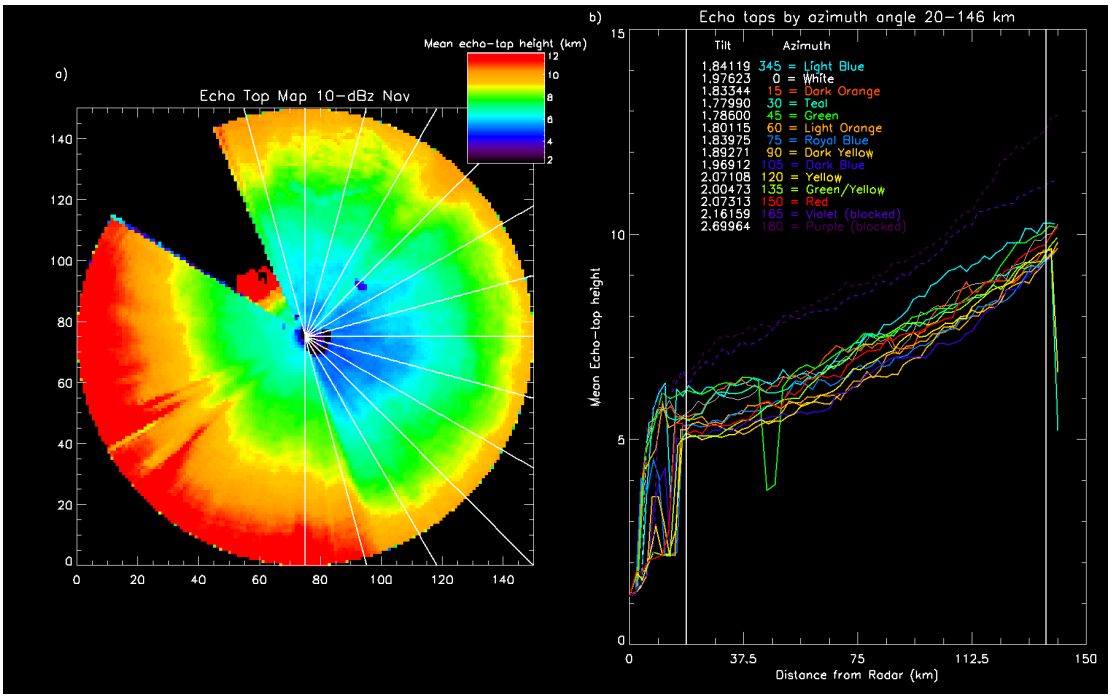

Figure 4.4: November echo-top plot with tilt correction. Same as Figure 4.3 except with a 0.75° tilt correction towards azimuth 285° applied.

shows the resulting corrected echo-top map for the month of November.

The penultimate stage of raw to NETCDF processing interpolates the files from polar to Cartesian coordinates using NCAR's REORDER. The result is a three-dimensional NETCDF file with 2-km horizontal resolution and 0.5-km vertical resolution. The radius of influence is set to 1.5 km in the horizontal directions and 1.2 km in the vertical direction. There are 40 vertical levels, ranging from a 0.5 km constant altitude planned position indicator (CAPPI), up to a 20 km CAPPI.

Lastly, SQI filtering is performed again. During the conversion to Cartesian coordinates, some of the fields get blended onto nearby points resulting in some false echo reappearing; thus a second round of SQI filtering is necessary. The filters are set to 0.225 at and below 5 km and 0.15 above 5 km. These values are set slightly higher than those used during the quality control algorithm because of the

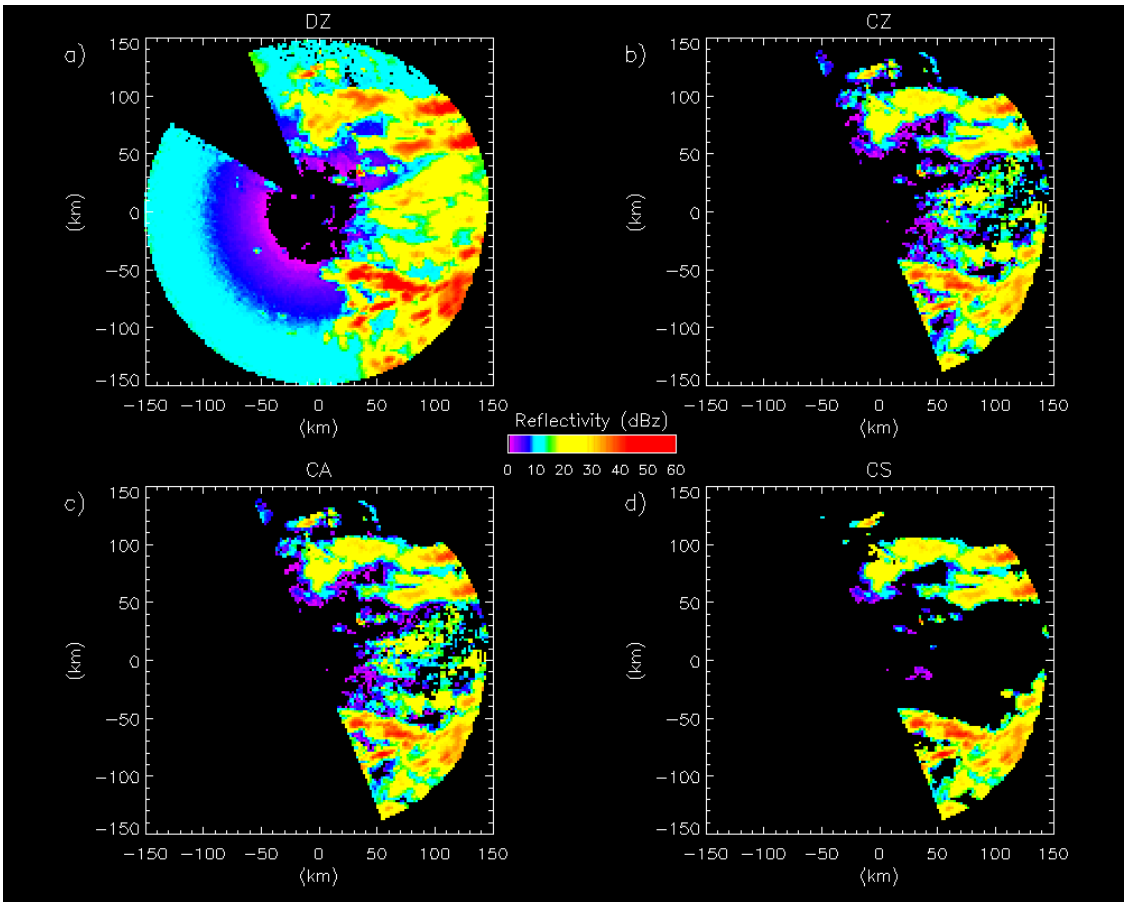

Figure 4.5: Three-km horizontal cross section raw to NETCDF quality control processing example from 14:36 UTC 27 Nov 2011. a) DZ field: raw data field collected by SMART-R. Wedge missing is area in front of truck cab that is not radiated. b) CZ field: DZ data that is run through quality control algorithm and has had -8 dB calibration offset applied. Mask from 338° to 158° applied. Mask also applied in c) and d). c) CA field: CZ data that is run through attenuation correction algorithm. d) CS field: CA data that is run through SQI filter to remove second trip echo and other false signatures.

transformed coordinate system. Figure 4.5 shows an example of how reflectivity data on a particular file changes throughout the raw to NETCDF processing. Table 4.2 shows the total number of NETCDF files created for each day. A day with no errors or shutdowns will have 144 files.

Table 4.2: Number of NETCDF files created by UTC date. A day with no interruptions will have 144 files.

Date	Files	Date	Files	Date	Files	Date	Files
2 Oct	139	4 Nov	144	7 Dec	144	9 Jan	86
3 Oct	139	5 Nov	144	8 Dec	132	10 Jan	144
4 Oct	142	6 Nov	144	9 Dec	144	11 Jan	144
5 Oct	144	7 Nov	142	10 Dec	144	12 Jan	144
6 Oct	100	8 Nov	140	11 Dec	135	13 Jan	140
7 Oct	122	9 Nov	143	12 Dec	144	14 Jan	144
8 Oct	144	10 Nov	141	13 Dec	144	15 Jan	140
9 Oct	144	11 Nov	144	14 Dec	129	16 Jan	144
10 Oct	144	12 Nov	137	15 Dec	144	17 Jan	144
11 Oct	144	13 Nov	144	16 Dec	143	18 Jan	144
12 Oct	144	14 Nov	144	17 Dec	144	19 Jan	144
13 Oct	142	15 Nov	144	18 Dec	144	20 Jan	144
14 Oct	144	16 Nov	144	19 Dec	144	21 Jan	144
15 Oct	137	17 Nov	144	20 Dec	144	22 Jan	138
16 Oct	144	18 Nov	144	21 Dec	144	23 Jan	144
17 Oct	144	19 Nov	140	22 Dec	143	24 Jan	144
18 Oct	144	20 Nov	144	23 Dec	144	25 Jan	144
19 Oct	144	21 Nov	143	24 Dec	144	26 Jan	144
20 Oct	144	22 Nov	144	25 Dec	118	27 Jan	144
21 Oct	144	23 Nov	144	26 Dec	143	28 Jan	144
22 Oct	144	24 Nov	144	27 Dec	144	29 Jan	144
23 Oct	142	25 Nov	144	28 Dec	144	30 Jan	144
24 Oct	144	26 Nov	132	29 Dec	141	31 Jan	144
25 Oct	144	27 Nov	144	30 Dec	144	1 Feb	144
26 Oct	143	28 Nov	144	31 Dec	144	2 Feb	144
27 Oct	144	29 Nov	144	1 Jan	144	3 Feb	143
28 Oct	141	30 Nov	144	2 Jan	144	4 Feb	143
29 Oct	140	1 Dec	144	3 Jan	144	5 Feb	144
30 Oct	141	2 Dec	144	4 Jan	144	6 Feb	137
31 Oct	143	3 Dec	144	5 Jan	144	7 Feb	141
1 Nov	129	4 Dec	144	6 Jan	144	8 Feb	144
2 Nov	142	5 Dec	144	7 Jan	128	9 Feb	144
3 Nov	141	6 Dec	144	8 Jan	56		

4.3 NETCDF to 3DPRODUCTS

Once three-dimensional Cartesian files based on interleaved volume scans are available in NETCDF format, a variety of products can be produced. Figure 4.6

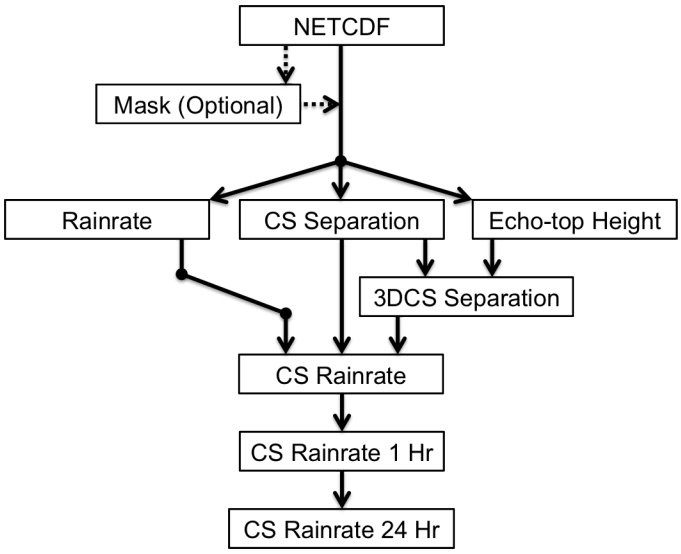

Figure 4.6: Processing stream to convert NETCDF files into 3DPRODUCTS.

depicts the processing stream to create these products. As an optional first step in the processing, a radial and sector mask (Sec. 4.3.1) can be applied to the NETCDF file to remove any unwanted sectors (for instance the region where SMART-R experiences significant blockage) or to remove data both close or far away from the radar.

From the 10-min NETCDF file (masked or unmasked), three products are produced: a rainrate map (Sec. 4.3.2), a convective/stratiform map using the Steiner et al. (1995) separation algorithm (Sec. 4.3.3), and an echo-top height map (Sec. 4.3.4). Additional products can then be produced. For example, a convective/stratiform map with height dependency, which uses echo-top height data to refine the original convective/stratiform map is the first 'joint' product. This is referred to as the three-dimensional convective/stratiform separation (3DCS) map (Sec. 4.3.5).

From here, further joint products are produced. These include rainmaps separated into convective and stratiform components using either the Steiner et al. (1995) method or CS3D (Sec. 4.3.6). Finally, hourly and daily rainrate maps, which combine the 10-min convective/stratiform rainmaps, are created (Secs. 4.3.7 and 4.3.8).

Computer programs to create the products were written in C Programming language. Most programs utilize three function library programs created by the University of Washington (UW; arrayutil.cc, assortutil.cc, zedcdf.cc). The versions of the function library programs being used were last updated in 2000 (Brodzik, personal communication, October 2011). The author of this thesis wrote all product programs unless otherwise noted.

4.3.1 Mask

The optional mask program reads in a single NETCDF file and applies a minimum and maximum radius to the data as specified by the user. The user can also remove an angular sector of the data by specifying a start and end angle. With 0° pointing due north, the user must enter the start angle of the sector to be removed beginning from 0° and moving clockwise. For instance to remove the top half of the map, the start angle input would be 270° (start angle when moving clockwise from 0)° and the end angle input would be 90°. The output of this program is in the same Cartesian format of the original NETCDF file, with the radial and sector areas designated for removal assigned a missing value number. Figures 4.5 b-d show the mask used for the majority of the analysis in Chapter 5. Variations of this mask can be used when comparing SMART-R statistics to observations from S-PolKa and the DOE AMF2, which have different spatial sampling.

4.3.2 Rainrate

The rainrate algorithm is a modified version of code written by Stacy Brodzik of the UW in 2001. The rainrate algorithm reads in a single NETCDF file and converts the three-dimensional volume scan into a two-dimensional plot at a specified

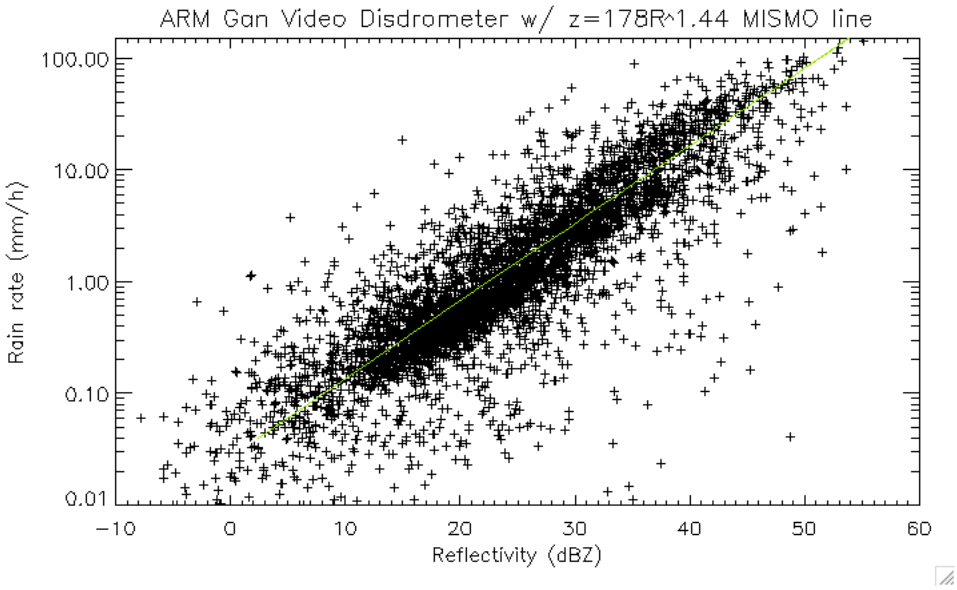

Figure 4.7: DYNAMO disdrometer data with Z-R relation a=178 and b=1.44 indicated by the green line.

CAPPI level based upon user input. An input is available for a reflectivity calibration offset; however, in most cases, the calibration performed in the processing from raw to NETCDF is sufficient. The user also designates an "a" and "b" value for the reflectivity-rainrate (Z-R) relationship (Eq. 4.1):

$$Z = aR^b \tag{4.1}$$

The values selected for a and b were 178 and 1.44, respectively. These were the values used during MISMO (Katsumata, personal communication, October 2011). DOE ARM mobile facility 2 (AMF2) video disdrometer observations from Gan matched well with the MISMO data (Figure 4.7), thus the values for a and b were kept the same.

A minimum map radius is also built into the algorithm as an input parameter. The maximum map radius is calculated through the algorithm by reading the

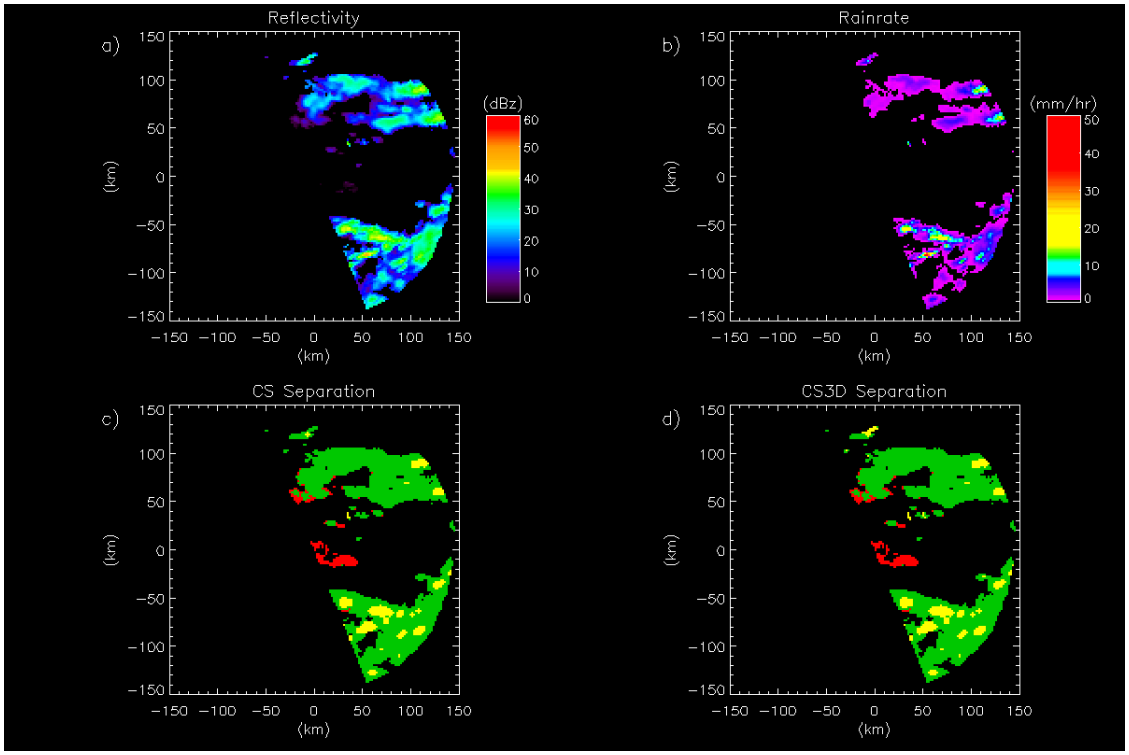

Figure 4.8: Three-km horizontal cross section product example from 14:36 UTC 27 Nov 2011. a) Reflectivity: Same as Figure 4.5c with a different color scale. b) Rainrate as calculated by rainrate algorithm in mm/hr. c) Steiner et al. convective/stratiform separation. Red indicates weak rain, green indicates stratiform rain, and yellow indicates convective rain. d) 3D convective/stratiform separation.

NETCDF file data. The rainrate algorithm will output one NETCDF file, which contains two variables; a rainrate map calculated through the algorithm and a reflectivity map with the calibration offset applied. Both maps are two-dimensional plots at fixed height at the specified CAPPI level. Figures 4.8a and b show an example reflectivity and rainrate map at 3 km from 14:36 UTC 27 November 2011.

4.3.3 Convective/Stratiform Separation

The convective/stratiform separation algorithm (CS) is a slightly modified version of the convective/stratiform algorithm used by UW. It reads in a single NETCDF

file and creates a convective/stratiform separation map at a user-specified CAPPI level. The code is primarily based on the Steiner et al. (1995) scheme, which was a modified version of the Churchill and Houze (1984) scheme. As specified by Steiner et al., convective rain regions are determined by three criteria:

- Intensity - Any pixel that has a reflectivity value above 40 dBz is classified as a convective center.

- Peakedness - Any pixel not classified as convective by the intensity criteria, but that has a reflectivity greater than the mean background intensity is classified as convective. The mean background intensity (Z_{bg}) is determined by averaging the intensity of the non-zero reflectivity values within 11 km of the specified pixel. Whether a pixel is to be classified as convective under this criterion is determined by the line in Figure 4.9. The line is the same function (Eq. 4.2) used in Yuter and Houze (1998), where values for a and b have been tuned to 8.5 and 52 respectively by subjectively comparing SMART-R observed CS maps, reflectivity maps, and reflectivity cross sections to select values that produce the most realistic results; e.g. making sure a region with bright band signature is not categorized as convective.

$$\Delta Z = a * \cos\left(\pi Z_{bg}/2b\right) \tag{4.2}$$

- Surrounding Area - For convective centers identified by either the intensity or peakedness criteria, a surrounding radius is also classified as convective based upon the intensity of each convective pixel.

Rain is classified as convective by meeting any of the convective criteria above, weak if the reflectivity is below a user determined weak threshold (set to < 5 dBz), or no

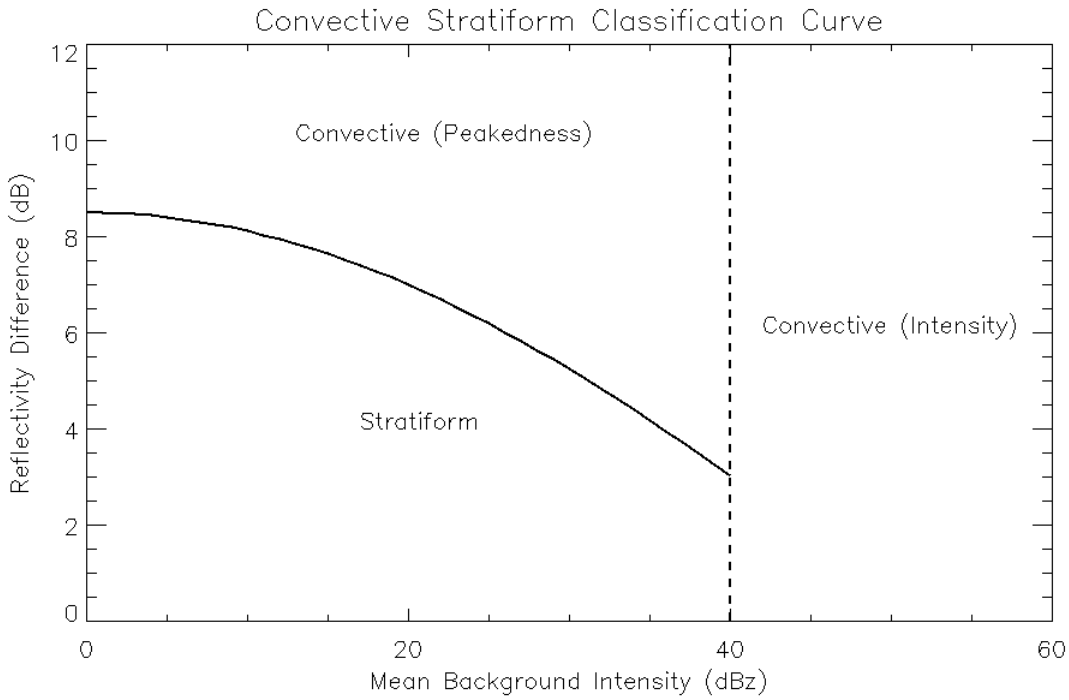

Figure 4.9: Convective/stratiform separation curve. Curve given by Equation 4.2 that separates convective cores from stratiform rain using the peakedness criteria. All reflectivity greater than 40 dBz is classified as a convective core by the intensity criteria.

rain echo if the reflectivity is below a user determined no rain echo (set to $<$ -50 dBz). Any remaining echo after these classifications is categorized as stratiform.

The algorithm also applies a minimum and maximum map radius in the same method described for the rainrate algorithm. The output of this algorithm is a NETCDF file containing the following rain classifications:

- 0 = no rain or below no rain threshold
- 1 = stratiform rain
- 2 = convective rain
- 3 = weak echo

Figure 4.8c shows an example of the CS algorithm.

4.3.4 Echo-top Heights

The echo-top height algorithm reads in a single NETCDF file and produces a NETCDF output file with four echo-top height maps (in km) for four different user-selected dBz thresholds (e.g., 10, 20, 30, and 40 dBz). The algorithm applies a minimum and maximum map radius in the same method as described for the rainrate algorithm. There is also an option to put in a calibration offset.

The algorithm is hard coded up for a SMART-R NETCDF file, which has 40 CAPPI levels ranging from 0.5 km to 20.0 km and with 0.5 km spacing, but can be easily modified to accommodate radar files with different height spacing and levels. The algorithm starts at the highest level (level 40 or 20 km) and for each pixel, if there is an echo exceeding the specified echo-top threshold, that pixel is assigned a 20 km value. The next level (19.5 km) is then read in, and any pixel column that was not assigned a height classification at the 20-km level is then eligible to be assigned a value of 19.5 km if the reflectivity of a pixel exceeds the echo-top threshold. This process is continued through the lowest CAPPI level. Any pixel within the specified region not having a reflectivity value above the threshold within the column is assigned a value of 0 km. This procedure is repeated for all four requested echo-top threshold values. Figure 4.10b shows an example of the echo-top height algorithm.

4.3.5 Three-dimensional Convective/Stratiform Separation

It became evident through examining separation maps of the CS algorithm that some misclassifications were occurring. The three-dimensional convective/stratiform (3DCS) algorithm attempts to reduce these errors. It reads in the modified Steiner

et al. convective/stratiform separation and uses reflectivity data from the rainrate output file and echo-top height data from the echo-top height output file to make changes to some of the rain type classifications.

The 3DCS algorithm was deemed necessary as the Steiner et al. algorithm appeared to have a bias towards stratiform rain, i.e., shallow and mid-level precipitation with obvious convective features were almost exclusively being categorized as stratiform rain because of their weak reflectivity. The 3DCS algorithm improves the convective/stratiform separation by classifying more of the shallow- and mid-level rain as convective. In the tropics, almost all stratiform rain generally forms out of regions of deep convection, not on its own, and thus it was unrealistic when the original algorithm classified spotty small areas of rain as stratiform (Houze, 1997; Schumacher and Houze, 2003).

The 3DCS algorithm does not change rain that was classified in the original separation as convective, weak echo, or no rain, nor does it change the classification of any rain within 20 km of SMART-R as the cone of silence directly above the radar limits echo-top data. Rain that was classified as stratiform, however, is sometimes changed to a convective classification in the 3DCS algorithm. First, in order for a pixel to be eligible for re-classification, there must be no echo signature at the point a set distance to the north, south, east, and west of that pixel. This 'isolation' parameter is intended to make sure the pixel is in fact isolated, and not part of a large, broad, stratiform region. After tuning, the 'isolation' parameter was set to 10 km; there are occasions where a truly isolated cell does fail this requirement and cannot be reclassified, however this does not appear to happen frequently.

For each pixel that passes the isolation assessment, if the original classification was stratiform and the 10-dBz echo-top height for that pixel in the column is greater than 9.0 km, that classification remains stratiform. However, if rain at the pixel was

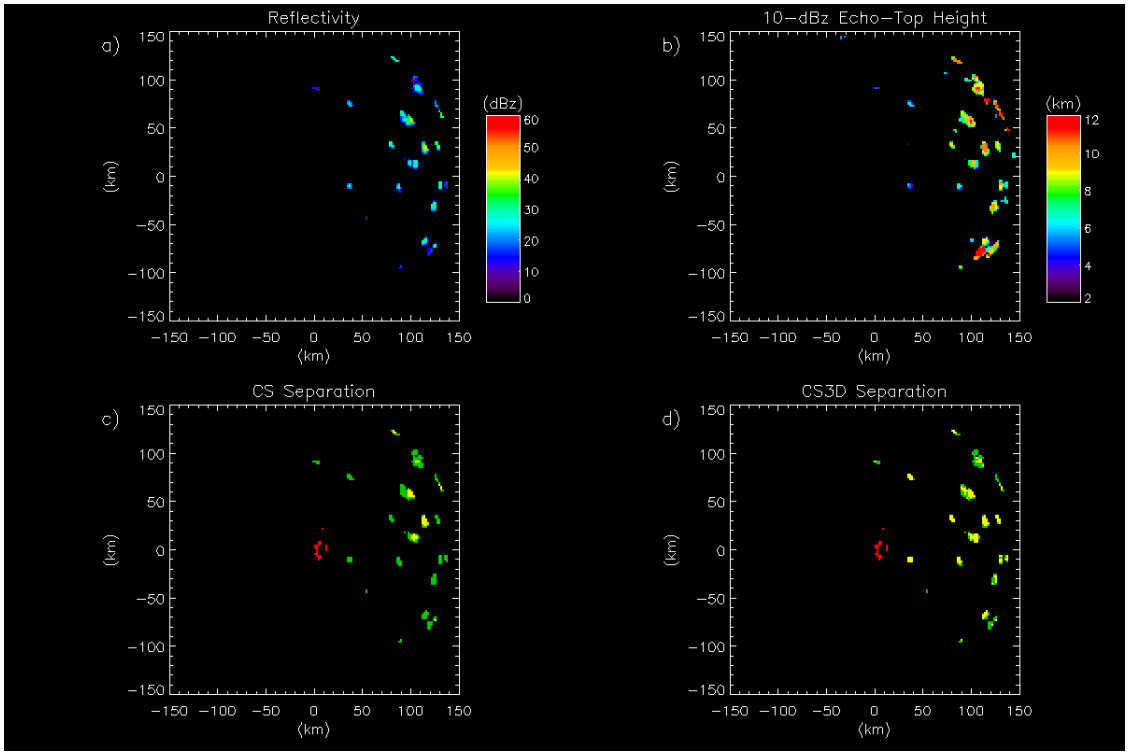

Figure 4.10: Three-km horizontal cross section product example from 03:26 UTC 9 Nov 2011. a) Reflectivity at 3 km. b) 10-dBz echo-top heights from 2-12 km. c) Convective/stratiform separation. Red indicates weak rain, green indicates stratiform rain, and yellow indicates convective rain. d) 3D convective/stratiform separation.

classified as stratiform and has an echo-top height less than or equal to 9.0 km, it is a candidate to be changed to a convective classifications. Nine km was chosen because a large majority of rain with echo-top heights below this level is developing convection, not lingering stratiform when combined with the isolation paramter.

An input parameter to the 3DCS algorithm is a shallow stratiform reflectivity threshold. If a stratiform pixel has an echo-top height less than or equal to 9.0 km and the reflectivity at the level of the separation is less than the threshold, the pixel keeps its stratiform classification. However, if the reflectivity is equal to or exceeds the threshold value, the pixel becomes reclassified as convective. Tuning of the algorithm resulted in a shallow stratiform reflectivity threshold set to 16 dBz. By

setting these thresholds, light reflectively on the edge of stratiform regions are less likely to be wrongfully categorized as convective; in the case that stratiform rain is below 9.0 km, it would still have to be greater than 16 dBz to be changed in addition to being isolated. While this modification to the Steiner et al. algorithm is not perfect, it does appear to improve the accuracy of convective/stratiform separations. The impact of using the 3DCS on the overall SMART-R convective/stratiform rain statistics will be addressed in Chapter 5.

The 3DCS algorithm produces a convective/stratiform separation map with the same number scheme as outlined for the Steiner et al. algorithm in Sec. 4.3.3. Despite its name, it is a two-dimensional map at a fixed height. Figures 4.8c and d show an example when the 3DCS algorithm does not modify the CS algorithm much. Figures 4.10c and d show an instance with lots of isolated shallow and mid-level convection that resulted in some classification changes.

4.3.6 CS Rainrate

The convective-stratiform (CS) rainrate algorithm masks the output file from the rainrate algorithm (Sec. 4.3.2) with the output from the CS (Sec. 4.3.3) and 3DCS algorithms (Sec. 4.3.5). The output from this algorithm produces a NETCDF file with six variables. The first output is a rainrate map, which includes all pixels that were labeled either convective or stratiform in the CS algorithm; pixels with either a weak echo or no rain echo classification are given a rainrate value of 0 mm/hr.

The second and third outputs are rainrate maps strictly containing only pixels with a convection classification or only pixels with a stratiform classification. As before, any pixel with a weak echo or no rain classification is given a rainrate value of 0 mm/hr. For the convective rainrate map, stratiform pixels are assigned a rainrate of

0 mm/hr and vice versa for the stratiform rainrate map. Outputs four, five and six are total rainrate, stratiform rainrate, and convective rainrate as produced by the 3DCS algorithm.

4.3.7 CS Rainrate 1 Hr

The CS Rainrate 1 Hr algorithm adds all of the 10-min CS rainrate files for each hour (Sec. 4.3.6) to create an hourly rainrate map of total, stratiform and convective rain in units of mm/hr. CS Rainrate 1 Hr outputs are only created for hours in which there is sufficient data to create an hourly plot; this is controlled by a mechanism in the master script which determines if there is a good enough data set for the hour.

Any hour that has all six 10-min files can obviously produce an hour file. To determine if an hourly file can be created when there are less than six 10-min files, a counting scheme has been devised which assigns the following values to each 10-min interval.

- 1 = Scan from 00-09 minute of each hour
- 2 = Scan from 10-19 minute of each hour
- 3 = Scan from 20-29 minute of each hour
- 4 = Scan from 30-39 minute of each hour
- 5 = Scan from 40-49 minute of each hour
- 6 = Scan from 50-59 minute of each hour

The numbers assigned to each file present for a specific hour are then added up; an hour with all six files has a value of 21 (1+2+3+4+5+6). The average value of the

data set [1,2,3,4,5,6] is 3.5 (Eq. 4.3), the standard deviation is 1.7 (Eq. 4.4), and the standard deviation of the mean is 0.69 (Eq. 4.5).

$$\bar{x} = \frac{x_1 + x_2 + ... + x_n}{N} \tag{4.3}$$

$$\sigma = \sqrt{\frac{\Sigma(x - \bar{x})^2}{N}} \tag{4.4}$$

$$\sigma_{mean} = \frac{1}{\sqrt{N}}\sigma \tag{4.5}$$

In order for an hourly file to be produced, the mean value of the available files must be within two standard deviations of 3.5. For instance, if scans 1, 2, 4 and 6 are present, and scans 3 and 5 are missing, the mean would be 3.25 ((1+2+4+6) / 4), which is within two standard deviations of 3.5. In fact, any hour with six, five, or four total scans, regardless what times they occur, meet this criterion. Also, all hours with only three scans also have a mean value within two standard deviations of the 3.5 mean value, except for hours which only have scans [1,2,3] or [4,5,6]. For these two occasions, as well as any hours with only 2, 1, or 0 scans, no hourly file is produced.

This procedure was decided upon for a few reasons. First, while a gap filling method could have been used to fill in missing scans, this would often incorporate scans from outside of a particular hour; sometimes well outside of an hour. As the weather was often observed to change very quickly at Addu Atoll, it did not seem reasonable to use data outside of an hour to create the hourly data files. For instance, if no files were produced for scans 3, 4, 5, and 6 in a particular hour, a common gap filling method would give each of those scans the same value, which would be determined by adding together the four previous and next scans and dividing by eight to get their average. Under this method the hourly file would be created with

the following data:

- 16.67% from Scan 1
- 16.67% from Scan 2
- 66.67% from gap filling (of which 50% is from out of the hour, and the remaining 16.67% comes from scans 1 and 2)

This is simply too much data from outside of the hour influencing the hourly statistics, and thus the counting scheme was chosen over a gap filling method to calculate hourly rain rates.

4.3.8 CS Rainrate 24 Hr

The CS Rainrate 24 Hr algorithm adds all of the CS Rainrate 1Hr outputs that were created for a specific day and creates a daily rainrate map of total, stratiform, and convective rain in units of mm/day. CS Rainrate 24 Hr outputs add together all hourly files created for the day, divides by the total number of input files, and multiples by 24 to give equal weight to each hour in the event there are not twenty-four hourly files available for the day.

5. RESULTS

5.1 Introduction

Rain and echo-top statistics will be presented as time series separated into months to observe the evolution of individual MJO events. A comparison between rainrates observed by SMART-R and S-PolKa will also be made. Then statistics will be composited by MJO phase to provide a climatology of MJO evolution in the central Indian Ocean and may foster the growth of a more localized MJO index. Lastly, the role of moisture and shear in the environment will be assessed through echo-top statistics and sounding data with the hope of better understanding the initiation processes of the MJO.

5.2 Monthly and Full Campaign Analysis

Section 5.2.1 will present a statistical survey of rainfall rates and areal coverage month by month and for the entire campaign. Section 5.2.2 investigates 10- and 40-dBz echo-top heights as they progress through time. Both sections will also discuss the difference between using the CS and 3DCS algorithms.

5.2.1 Rainfall and Areal Coverage statistics

Figure 5.1 shows the time series for area-averaged rainfall between azimuth angles 338° - 158° and out to a radial distance 150 km from SMART-R. Lines for total (solid), convective (dashed), and stratiform (dotted) rain are plotted. Convective and stratiform lines are from the 3DCS algorithm; CS algorithm lines almost exactly mirror their 3DCD counterparts. Vertical lines are used for easy identification of

MJO phase given by the Wheeler and Hendon index. As seen in Figure 5.1, the MJO was active in the central Indian Ocean twice during the campaign; first during mid and late October, and a second instance roughly during the same time period of November. As expected, rainfall amounts appear highest during phases 1 and 2 when the MJO is over the western and central Indian Ocean. Following the MJO event in November, the MJO remained in phases 4 through 7 until the campaign was suspended.

For the October event, a buildup in rainfall becomes evident during phase 8, with the highest daily rainfall values occurring during phase 1. Phase 2, while longer than phase 1, experiences slightly less in terms of daily rainfall maximum. Nonetheless,

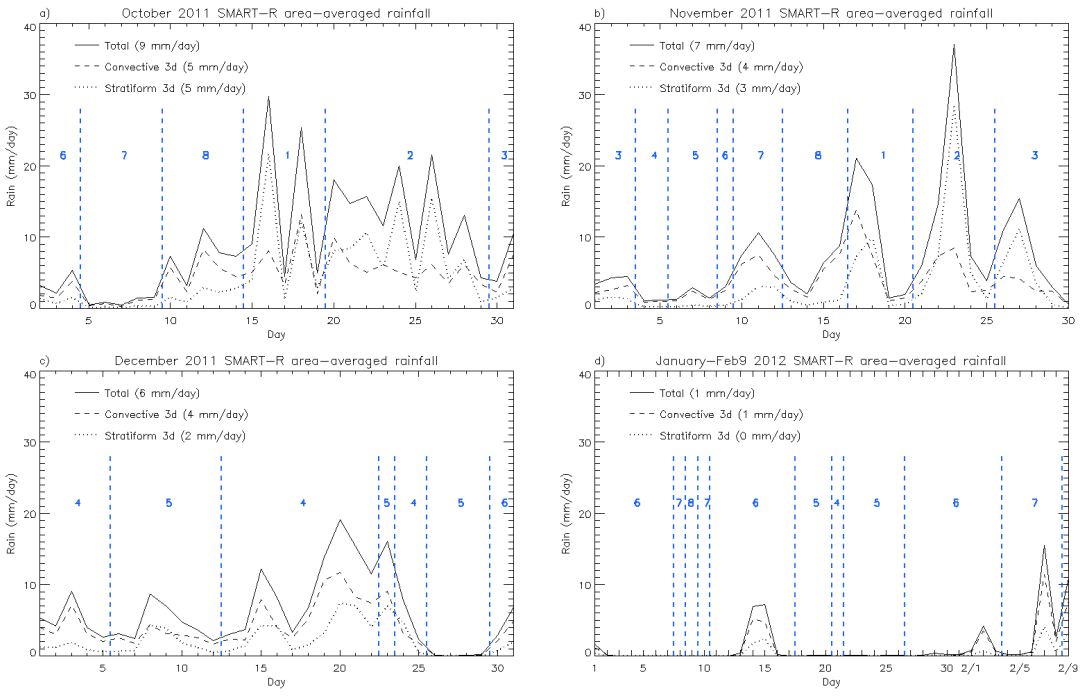

Figure 5.1: SMART-R area-averaged rainfall rates. Rainfall rates broken up by month for a) October, b) November, c) December, and d) January-February. Solid line indicates total rainfall, dashed convective rainfall, and dotted stratiform rainfall. For convective and stratiform rain, the 3DCS lines are plotted; the CS rainfall lines are nearly identical. Vertical dashed lines indicate MJO phases based on the Wheeler and Hendon index. Monthly averages are shown in the legend.

large rainfall occurs during this phase. By phase 3, the MJO begins to become suppressed with 31 October being the last day with total rainfall above 10 mm/day until the beginning of initiation for the November event.

The November event experiences buildup in phase 7, a phase earlier than the October event. In addition, phase 8 has a noticeable dip in rainfall before enhancing and ushering in phases 1 and 2. Unlike the October case, the November MJO experiences its maximum rainfall day during phase 2. As November closes and December begins, phases 3 and 4 show a decrease in rainfall as suppression sets in.

Following the November MJO event, rainfall begins to increase in mid December with the MJO oscillating back and forth between phases 4 and 5. This is unexpected behavior; convection should be fairly suppressed in the central Indian Ocean during these phases. Current thinking by the wider community is that this rain is not associated with an MJO event, rather a strong Kelvin wave moved through the western hemisphere that resulted in nonstandard convection in the Indian Ocean and caused the MJO index to fluctuate between phases. More analysis into how this could alter results based on phase will be given in Sec. 5.3. January was very dry over Gan with rainfall enhancement occurring during phase 7 in early February before the next MJO event, which occurred after operations ended.

Two intriguing rainfall patterns are observed during the time series. First, in the October event, a minimum in daily rainfall is usually sandwiched between two maxima (i.e., a 2-day cycle). This happens 10 - 12 October, and 16 - 29 October. Despite the magnitude of the oscillation not being as strong from 20 - 22 October, the 2-day pattern remains intact.

The other rainfall pattern observed is one of a maximum observed every four to seven days beginning in mid November and continuing through mid December. The days 11, 17, 23, 27 November and 2, 8, 15, and 20 December all contain a

maximum of rainfall (there is a secondary maximum on 1 December as well, but it is significantly smaller than the other ones).

These patterns are interesting because they suggest a need for a recharge after a significant rain event, yet they occur on very different time scales. While in October there seems to be only a one day recharge, November and December experience much longer periods for recharge with a few days of decreasing rain before hitting a minimum, followed by a build up until reaching another maximum. While it is impossible to extrapolate what occurred after 9 February, the pattern of a single day recharge appears to be taking place 7 - 9 February as the MJO transitions from phase 7 into 8 as an active MJO begins to develop in the western Indian Ocean.

The time series also reveals an interesting relationship between convective and stratiform rainfall. Convective rain is the dominant contributor to total rainfall during the suppressed phases of the MJO, however, during the active phases (1 and 2) and phase 3 for the November case, stratiform rain consistently is the larger supplier of rain each day. These results are consistent with Lin et al. (2004), which used TRMM PR data to show that stratiform precipitation lags convective precipitation by several days, and that a larger stratiform rain fraction occurs during the active MJO phases. This would appear to be evidence that organized convective clouds are a necessary condition for stratiform rain (e.g., Houze, 1997); during inactive phases where convection is stymied, little stratiform rain is produced.

However, as illustrated in Figure 5.2, which shows percent area of echo coverage, there is not one day that experiences more coverage from convective clouds than stratiform clouds over the duration of the campaign. Even in the periods when convective rain is dominant in terms of rainfall amount, stratiform rain covers a significantly larger area. In fact, despite small daily fluctuations from 1-4% on days with rain, occasionally approaching five percent coverage in phases 1 and 2. This is

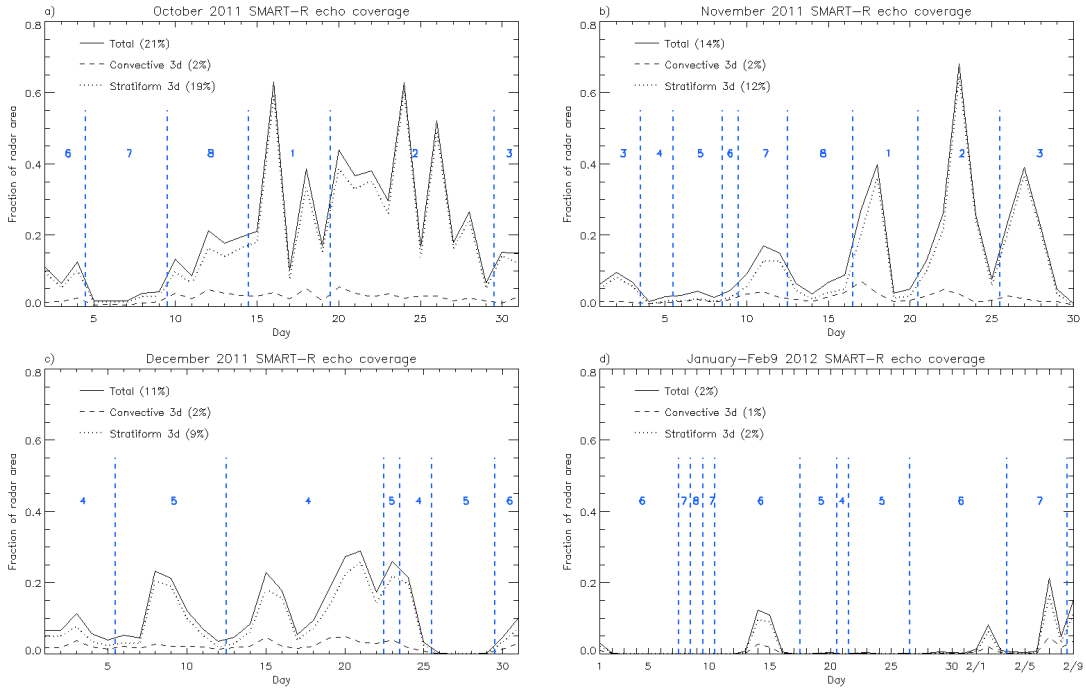

Figure 5.2: SMART-R percent areal coverage by rainfall type. Same as Figure 5.1 except showing percent areal coverage by rainfall type.

similar to the findings of Yuter and Houze (1998), which used airborne radar data from the Coupled Ocean-Atmosphere Response Experiment of the Tropical Ocean and Global Atmosphere programme (TOGA COARE) in the Western Pacific to show that percent areal coverage of convection did not vary much based on mean infrared (IR) temperature in a fine grid (24 km x 24 km) and was generally below 5% at coarse grid scales (240 km x 240 km); i.e. convective areal percentage stayed roughly constant regardless of the type of convection and was rarely covered a significant portion of the domain.

On the other hand, stratiform echo coverage closely mirrors total echo coverage regardless of MJO phase. This, coupled with the results above would seem to indicate that while convective and stratiform rain are always present, stratiform rain is fairly weak when the MJO is suppressed. There is no clear connection between con-

vective and stratiform area percentage; this agrees with results from other tropical ocean campaign findings such as TOGA COARE (Yuter and Houze, 1998) and the Tropical Pacific Warm Pool International Cloud Experiment (TWP-ICE) (Frederick and Schumacher, 2008) in Darwin, Australia. It is not until active phases of the MJO that the stratiform rain is strong enough to surpass convective rainfall despite always having a significantly larger areal coverage as compared to convective rain.

A summary of total rainfall amounts and areal echo coverage, in addition to statistics from the CS and 3DCS algorithms, can be found in Tables 5.1 and 5.2. October had both the largest rainfall amount and percent areal coverage, but also had the least amount of echo reclassified as convective. A factor for this may be extraneous data as a result of not filtering out low SQI values until 28 October 2011. Because the areal convective percentage is somewhat in the neighborhood of values for November and December, it is possible that some second trip echo or other false echo was not removed in October and resulted in the increased areal coverage, most of which was in the stratiform classification. November and December have larger convective reclassification percentages, i.e., approximately a four and three percent increase for rainfall respectively, and a 30 and 22 percent increase for echo coverage. Given that October and November are easy to compare since both have an MJO event, this is clear evidence that the removal of second trip echo is an important factor for reclassifying convective rain with the 3DCS algorithm. Reclassification values

Table 5.1: SMART-R rainrate statistics (mm/day).

Month	Total	Conv	3D Conv	Strat	3D Strat	Conv:3DConv Δ
Full Campaign	5.6	3.1	3.1	2.6	2.5	3.2 %
October	9.1	4.4	4.5	4.7	4.6	1.5 %
November	7.2	3.7	3.8	3.5	3.4	4.1 %
December	6.1	3.8	3.9	2.3	2.2	3.1 %
Jan-Feb	1.3	0.9	1.0	0.4	0.4	6.3 %

Table 5.2: SMART-R area rain statistics (%).

Month	Total	Conv	3D Conv	Strat	3D Strat	Conv:3DConv Δ
Full Campaign	11.2	1.4	1.8	9.8	9.5	22.1 %
October	21.1	2.2	2.5	18.9	18.7	11.8 %
November	13.9	1.8	2.3	12.1	11.6	30.5 %
December	10.9	1.7	2.1	9.2	8.8	22.1 %
Jan-Feb	2.1	0.4	0.5	1.7	1.6	37.2 %

are even larger in January; this may be a consequence of the period being very dry and the MJO being in suppressed phases. Shallow convection should constitute a larger percentage of clouds during this period, thus a higher reclassification value is expected.

5.2.2 Echo-top Observations

All echo-top plots have, in addition to the 180-degree mask seen in Figure 4.8, a radial mask that removes the 20 km closest to the radar and everything beyond 146 km from the radar. The inner 20 km are removed because of the cone of silence directly above the radar. Echo-top statistics are not accurate here because the radar cannot see very high within that radius. The outside annulus is removed because the echo-top statistics appeared to have a strange edge effect that could be due to beam geometry; echo-top height values were skewed much higher or lower along the 150 km edge than in regions adjacent to it.

Figure 5.3 shows the evolution of 10-(colored contours) and 40-(black contours) dBz echo tops with respect to time and height for each month. Evident prior to both the October and November MJOs is a low total count of echo tops, as well as a lower vertical structure of echo tops, which gradually builds up as onset occurs. This supports Johnson et al. (1999) in regards to low- and mid-level clouds preceding deeper clouds, and mirrors the Lau and Wu (2010) study which found lower clouds

during suppressed MJO phases gradually become deeper as active phases moved into the region of study. However, while the October case is characterized by limited echo tops in phase 7, with buildup into phase 8 and with a maximum in phase 1, the November case has a series of echo top peaks that begins in phase seven and follows the four to seven day rainfall pattern seen in Figure 5.1. Over the entire campaign, the top contour of the 10-dBz echo tops mimics the shape of total rainfall and total percent areal coverage well. The 40-dBz echo top contours do not have as discernible of a shape; while with deep convective clouds extend vertically, reflectivity tends to drop off with height (DeMott and Rutledge, 1998; Lerach et al., 2010). Forty-dBz reflectivities will not occur more than a few km above the melting layer, where as

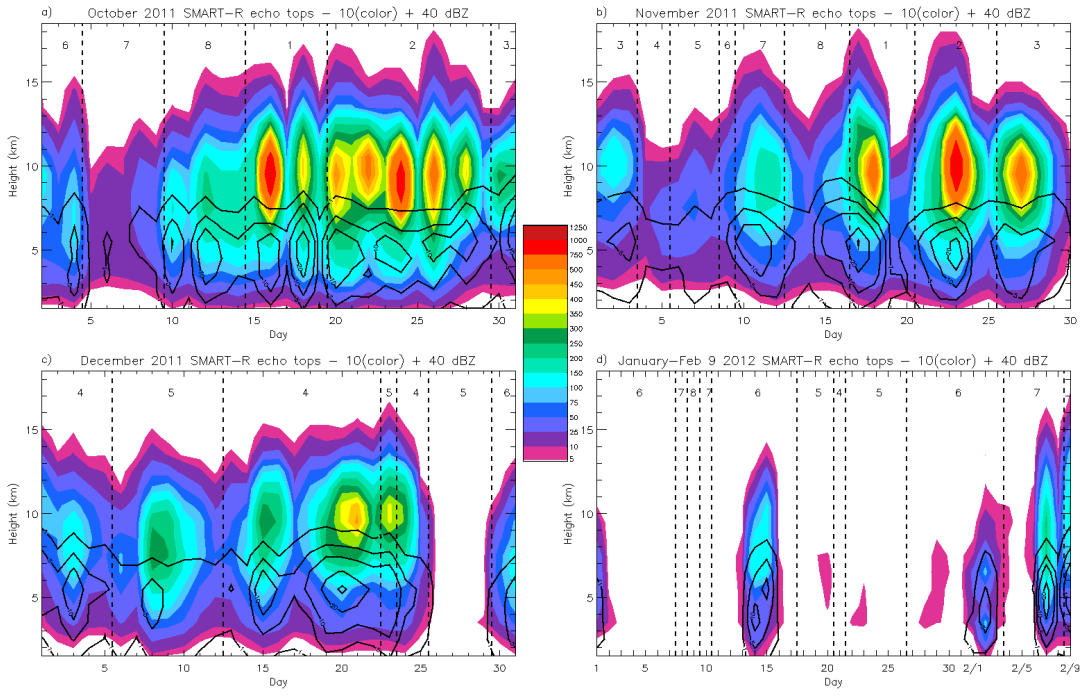

Figure 5.3: 10- and 40-dBz echo-top heights. 10-dBz (colored) and 40-dBz (black) contour plot of echo-top heights for a) October, b) November, c) December, and d) January-February. Black contours are labeled at 1, 5, 10, 20, 30... . Value indicated is average daily count for a full volume scan(10-min period) in the echo-top domain (annulus from 20 - 146 km between azimuth 338° - 158° per volume scan). Vertical dashed lines indicate MJO phase based on the Wheeler and Hendon index.

10-dBz reflectivites can extend into the stratosphere. Dry periods are also evident at the end of December and throughout much of January by the lack of significant 10-dBz echo coverage.

Figures 5.4a and b show the echo-top heights for November separated into stratiform only and convective only, using the CS algorithm. Two features are obvious from this breakdown. First, a majority of the 10-dBz echo tops are contributed by stratiform rain. Convective rain never exceeds the 150-count threshold, whereas stratiform rain is observed to exceed the 750-count threshold at times. Secondly, almost all 40-dBz contours are contributed by convective rain. This makes sense as the CS algorithm has an intensity threshold setting everything above 40-dBz to be convective. The few instances where 40-dBz contours occur in the stratiform rain regions are due to strong bright bands near the 0°C level (near 5 km) or fall streaks below 3 km.

The top outline of the 10-dBz contours is also of interest in comparing stratiform and convective rain to the area-averaged November rainfall in Figure 5.1b. The four significant rainfall events in November correspond to the 11th, 17th-18th, 23rd, and 27th, which occur in phases 7, 1, 2, and 3. Just as in Figure 5.1b where convective rain peaks during phase 1 (17-18 November event), the echo tops seen in Figure 5.4b appear to peak both in height and count during this time. Stratiform rain (Figure 5.1b) gradually builds up during the first two events and peaks during event three (phase 2). The same buildup appears in figure 5.4a as contours both increase with height and counts up to the phase 2 event. The results in Figures 5.1 and 5.4 show that the maximum in stratiform rain and echo tops follows the maximum in convective rain; this will be examined more by phase in Sec. 5.3.

Figures 5.4c and d show the echo-top heights for November separated into stratiform only and convective only, using the 3DCS algorithm. The only distinct differ-

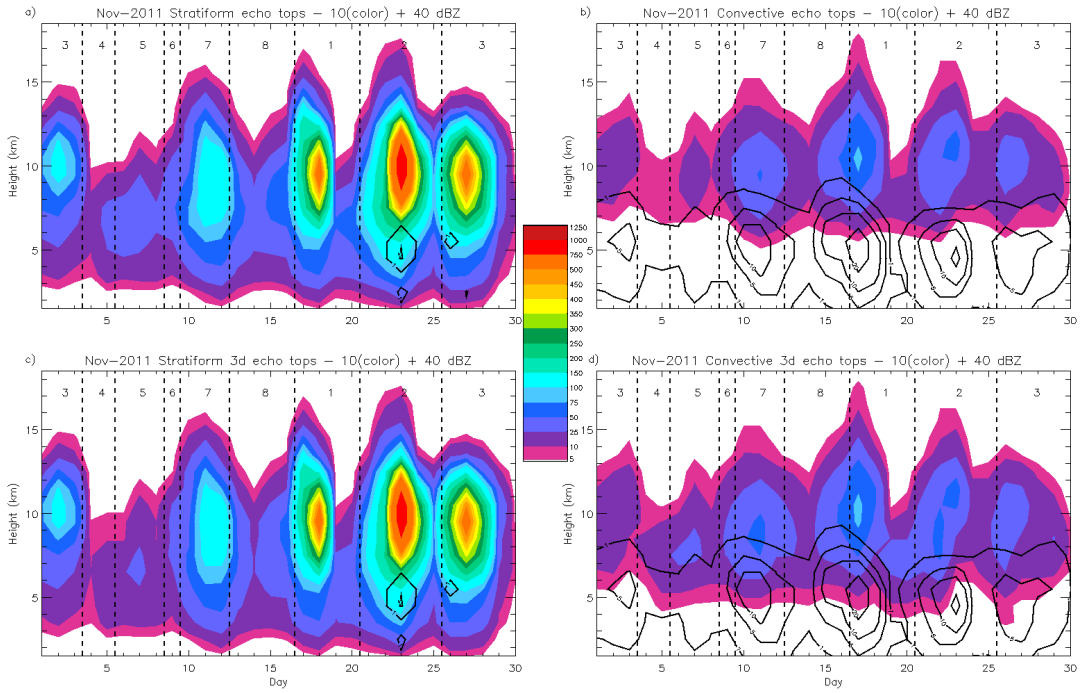

Figure 5.4: November echo tops. a) November stratiform echo tops from CS algorithm. b) November convective echo tops from CS algorithm. c) Same as a) except from 3DCS algorithm. d) Same as b) except from 3DCS algorithm. Contours and vertical dashed lines are the same as described in Figure 5.3.

ence between the CS and 3DCS plots is in the convective graphs; the 3DCS algorithm detects 10-dBz echo tops as low as 3.5 km (Figure 5.4d), whereas the CS algorithm detection of 10-dBz echo tops reaches a minimum at 5.5 km (Figure 5.4b). While the rain statistics presented in Tables 5.1 and 5.2 show only marginal changes between the CS and 3DCS algorithm, the echo-top histograms reveal the importance of the 3DCS algorithm. Without it, weaker convection in its initial stage of development is missed. Figure 5.4b is not a realistic view of the tropical environment, and while the 3DCS is not perfect and can still be improved upon, it draws a more accurate picture of the convective environment.

Figure 5.5 illustrates the importance of quality control on the radar data. The SQI field was not saved until 28 October; before this, significant of second trip echo

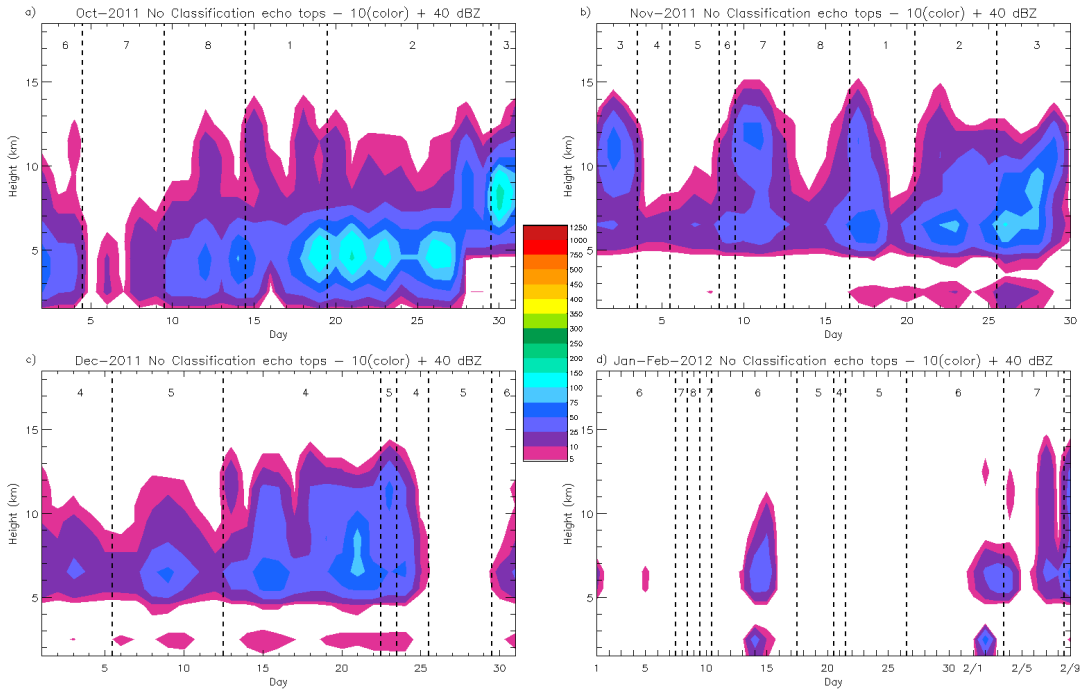

Figure 5.5: Anvil/clutter echo tops. Ten-dBz anvil/clutter echo-top heights (i.e., echo tops which were not classified as convective, stratiform, or weak) as determined by the CS algorithm for a) October, b) November, c) December, and d) January-February. Contours and vertical dashed lines are the same as Figure 5.3.

is apparent by the lack of white space under 5 km. Once SQI filtering is applied, only a few occasions record echo tops under 5 km, which can be attributed to extremely shallow clouds that did not have reflectivity return at the 3 km CAPPI that classified rain types. The contours above 5 km reveal non-precipitating anvil extending behind convective and stratiform rain. These counts represent areas that did not have a rain classification at 3 km, but had thick clouds in that column. As expected, these clouds, referred to as anvils, are most apparent on days featuring lots of convection. Appendix A has echo-top charts for October, December, and January-February.

5.3 SMART-R vs. S-PolKa

As discussed throughout this thesis, SMART-R experienced severe blockage towards the west. In order to provide validation that the results presented in this thesis are an accurate description of the region surrounding Addu, a comparison with the S-PolKa radar was performed. While S-PolKa also experienced some blockage towards the west, it was not nearly as severe as SMART-R's. Figure 5.6 shows SMART-R data (black lines) for October, November, and December plotted with S-PolKa data. The S-PolKa data set used is from 4 October - 31 December and is the preliminary data collected in the field with only real-time quality control performed.

The red line shows the rainrates seen by S-PolKa towards the west (west refers to the 158° - 338° sector SMART-R was blind to). Although there is some blockage that inevitably will lower their totals in this sector, it does not appear that there are many instances of increased rainfall in the west that did not occur in the east. In fact, there are only four days during this time period that S-PolKa saw more rain on its western half than eastern half. This validates the results of SMART-R in the sense that there were not many instances, if at all, that SMART-R recorded minimal rain, where in actuality all precipitation for the day was located to the west.

In addition, SMART-R's rainrates can be compared to what S-PolKa saw to the east (338° - 158° sector) as denoted by the green lines in figure 5.6. For days with rainrates under 15 mm/day, there is fairly good agreement between SMART-R and S-PolKa, however, on days with larger rainrates, S-PolKa rainrates are much higher. It is important to remember though that this S-PolKa data is not the final data set; the final data S-PolKa data set has lower rainrates amounts than indicated in the charts (Scott Ellis, personal communication, August 2012). The dashed orange line represents 75% of the S-PolKa east rainrates and appears to be in significantly

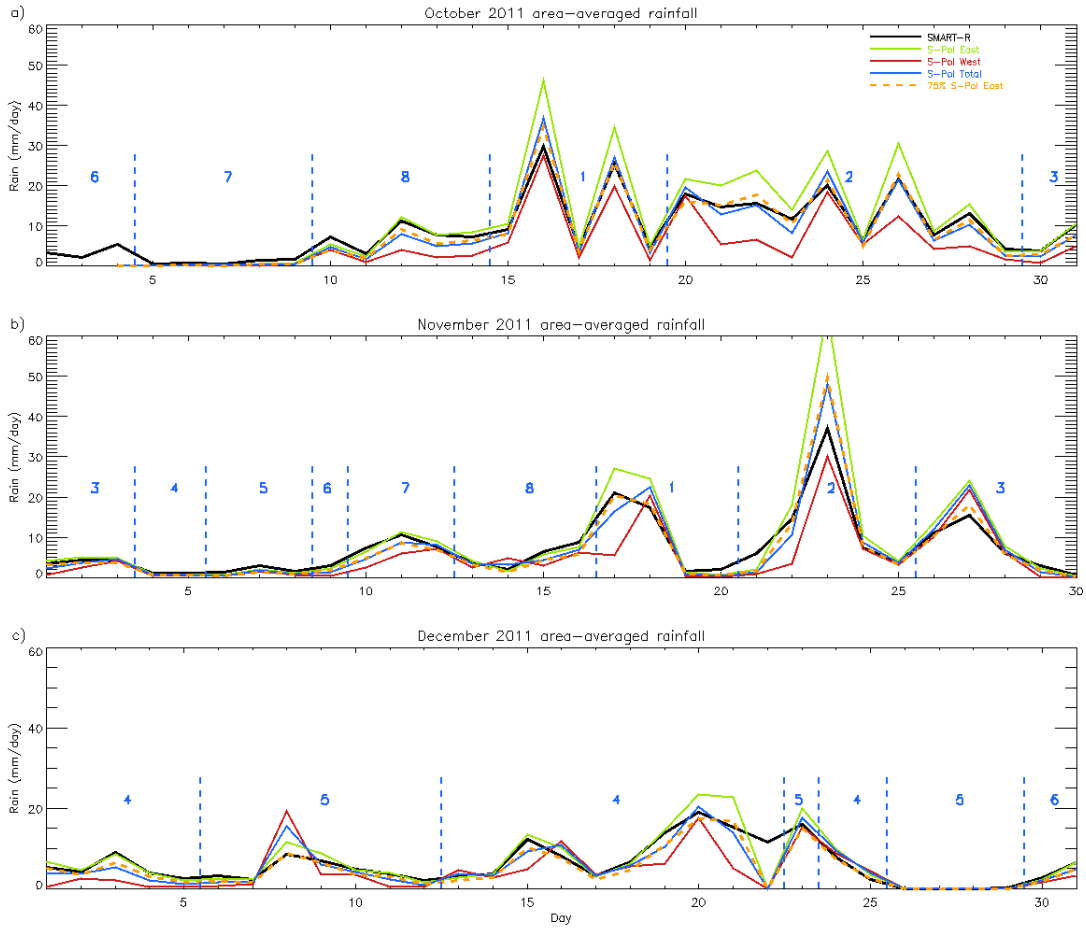

Figure 5.6: SMART-R / S-PolKa rain comparison. Separated by month for a) October, b) November, and c) December. SMART-R is indicated by black lines, S-PolKa's east region (338° - 158°) is green, S-PolKa's west region (158° - 338°) is red, and S-PolKa's entire domain is blue. Dashed orange line indicates 75% of S-PolKa's east region total.

better agreement than the green line with the exception of a few days, most noticeably November 23rd. Once the final S-PolKa data set is available, a more precise comparison can be made to determine how closely the SMART-R and S-PolKa data sets actually align.

5.4 Rain statistics by MJO Phase

The daily rain amounts from the 3DCS algorithm were composited using the Wheeler and Hendon Multivariate MJO index (white lines in Figure 5.7). A peak in convective rain (solid line) is observed during phase 1, which gradually decreases to a minimum in phase 6 with the exception of a spike during phase 4. Phases 7 and 8 show convective rain increasing back into phase 1. Stratiform rain (dashed lines) peaks in phase 2, decreases through phase 6, and then increases into phase 2. Of note regarding the stratiform rain is its sharp increase from phase 8 into phase 1, and that only in phases 1 and 2 does it have a rainrate higher than convective rain (phase 3 has approximately equal contributions from convective and stratiform rain). In addition, the peak in stratiform rain occurs one phase later (phase 2) than the peak in convection (phase 1), suggesting an increase of large mesoscale convective systems as the MJO matures.

The peak in convective rain in phase 4 appears to be out of place, most likely from the large-scale feature that caused the MJO index to fluctuate back and forth during December. The yellow lines in Figure 5.7 represent rain types composited by MJO phase excluding data from 13 - 25 December. This period corresponds to the time that the MJO reversed back into phase 4 from phase 5 and then oscillated between phase 5 and 4 once more. The result is a drastically different phase 4 composite, which fits the overall decreasing trend better than the original data set (white lines). In addition, the minimum convective phase is now phase 5, while the minimum stratiform phase remains phase 6. This duplicates the pattern seen in phases 1 and 2 where the convective peak occurs one phase prior to the stratiform peak; in this case, the minimum convective phase is followed by the minimum stratiform phase.

Further redactions from the full data set are shown by different color lines in

Figure 5.7. These correspond to different combinations of removing data when the MJO index moves backwards and oscillates between two phases. Marginal changes are observed, mostly in phases 4 and 5. One final way to decide which data to include is by using the amplitude of the Wheeler and Hendon MJO index. When the amplitude is less than 1.0, the MJO is considered to be weak. This occurs on 28 -

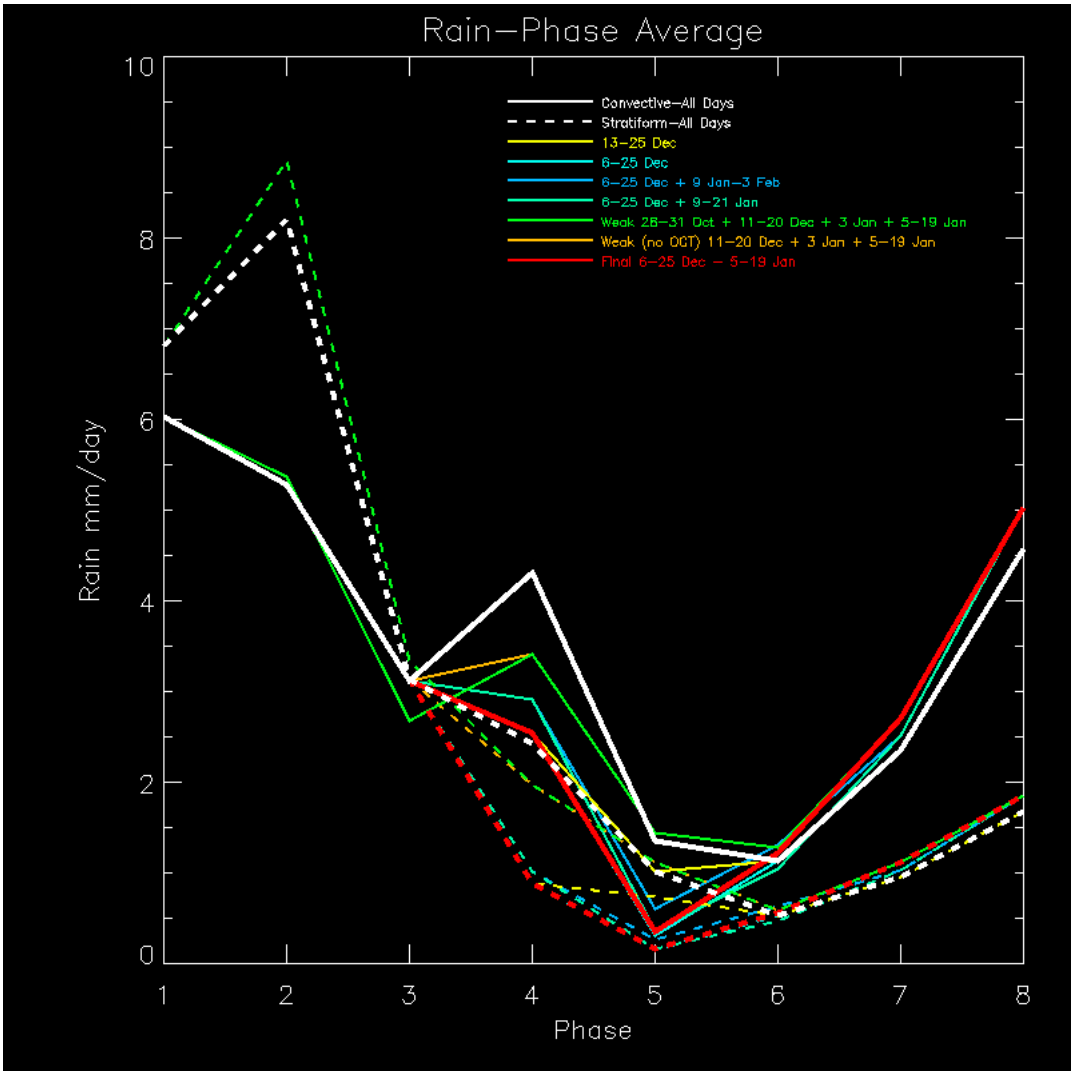

Figure 5.7: Convective/Stratiform rain by MJO phase. Convective rain is shown in solid lines, stratiform rain is shown in dashed lines. Colors represent different days being removed from data set as indicated by key. Black lines represent the full data set while red lines represented the truncated data set.

Table 5.3: Number of days each MJO phase occurred. Days are broken down into the full and truncated (not including 6 - 25 December and 5 -19 January) data sets based on the Wheeler and Hendon MJO index.

Phase	Full Data Set	Truncated Data Set
1	9	9
2	15	15
3	10	10
4	20	8
5	23	13
6	28	18
7	15	13
8	11	10
Total	131	96

31 October, 11 - 20 December, 3 January, and 5 - 19 January. The green lines in Figure 5.7 show the removal of just these dates. The most obvious changes from prior examples are a weakened phase 3 in the convective composite and strengthened phase 2 in the stratiform composite. However, removing data from the end of October because the Wheeler and Hendon MJO index is slightly below the weak threshold seems arbitrary, especially considering these dates occur in phases 2 and 3, precipitation is occurring as expected, and the precipitation appears to follow the expected decay towards the end of phase 2 into phases 3 and 4 that is expected as the enhanced MJO moves out of the central Indian Ocean.

Considering all of the above factors, and that any manipulation to the data set will have some amount of bias towards producing data that 'appears' correct, the removal of 6 - 25 December and 5 - 19 January seems to be the most appropriate adjustment to the data set; this is shown by the red lines in Figure 5.7, which capture a similar signal to some of the other plots, with the phase 4 convective accumulation being less than phase 3 convective accumulation the most important. The days removed from December correspond to the time when a large-scale dynamical feature other than

Table 5.4: Stratiform rain percent areal coverage. Coverage is separated into 'active' (phases 1-3), 'suppressed' (phases 4-8), and total (phases 1-8) phases based on the Wheeler and Hendon MJO index for full and truncated (not including 6 - 25 December and 5 -19 January) data sets.

Data Set	Active	Suppressed	All
Full	22.1 %	5.0 %	9.5 %
Truncated	22.1 %	3.8 %	10.3 %

the MJO is believed to have been the primary factor for precipitation. In addition, the MJO index was weak throughout the middle portion of the days, and thus it is acceptable to throw out this data. The January dates correspond to the time of a weak MJO signal in January, which also corresponds well to the time of the unusual MJO index backwards progression. For these reasons, this data set (hereafter referred to as 'truncated') is believed to be the most accurate in representing actual MJO behavior. Table 5.3 shows the number of days each phase occurred for the full and truncated data sets.

Finally, as discussed in Section 5.2.1, stratiform rain echo area generally mirrors total rain area (Figure 5.2). However, the areal coverage is increased greatly during 'active' phases (phases 1-3) of the MJO when compared to 'suppressed' phases (phases 4-8). Table 5.4 shows percent areal coverage of stratiform rain separated into active and suppressed phases for both the full and truncated data set. While active areal coverage is unaffected by the removal of days in the truncated set, suppressed areal coverage decreases while total (all phases) areal coverage increases. This result is expected as lots of rainy days from December were removed by using the truncated data set and the removal of those days increases the weight of the active phase areal coverage in the total calculation. The results of Table 5.4 illustrate that stratiform rain develops much more during active phases of the MJO compared to suppressed phases.

5.5 Diurnal Cycle

The diurnal rain cycle is investigated by grouping together the hourly files described in section 4.3.7. Figure 5.8 shows the diurnal rain cycle by hour for the full data set (solid lines) and for the data set where 6 - 25 December and 5 - 19 January are removed (truncated data set, dashed lines). Removing the dates that don't correspond to a 'normal' MJO has only a marginal effect on the results by slightly enhancing stratiform rain, especially during the late afternoon/early evening. In both cases, the largest peak in total rainfall is observed between 0300 and 0700 LT and is associated with increases in both convective and stratiform rain. A secondary peak is observed between 1100 and 1300 LT and is associated with an increase in convective rain. A third peak at 1700 UTC, which appears only in the truncated data set, is due to increased stratiform rain amounts.

These results match some of the findings of Jacobson (1976) and Gray and Jacobson (1977), which showed early morning and early afternoon peaks over large islands. However, the early afternoon had the larger peak in their study. Reasons for this discrepancy can possibly be attributed to Gray and Jacobson's use of rain gauge data on the islands rather than radar data used in the present study, which is almost exclusively open ocean; of SMART-R's 35343 km^2 domain, only approximately 60 km^2 is land, about 0.17%. If the lagoons of Addu and Huvadhoo Atoll (located 80 km north of Addu Atoll) are included as land area, the area jumps to approximately 3340 km^2 (3300 km^2 of which is the Huvadhoo lagoon), about 9.45% of SMART-R's domain. Possible explanations for the lower magnitude 1100-1300 LT maximum could be a diminished heat island effect when compared to studies just using land based data or diurnal variations in SST similar to the findings of Johnson et al. (2001) in TOGA COARE. They detected an afternoon maximum in SST

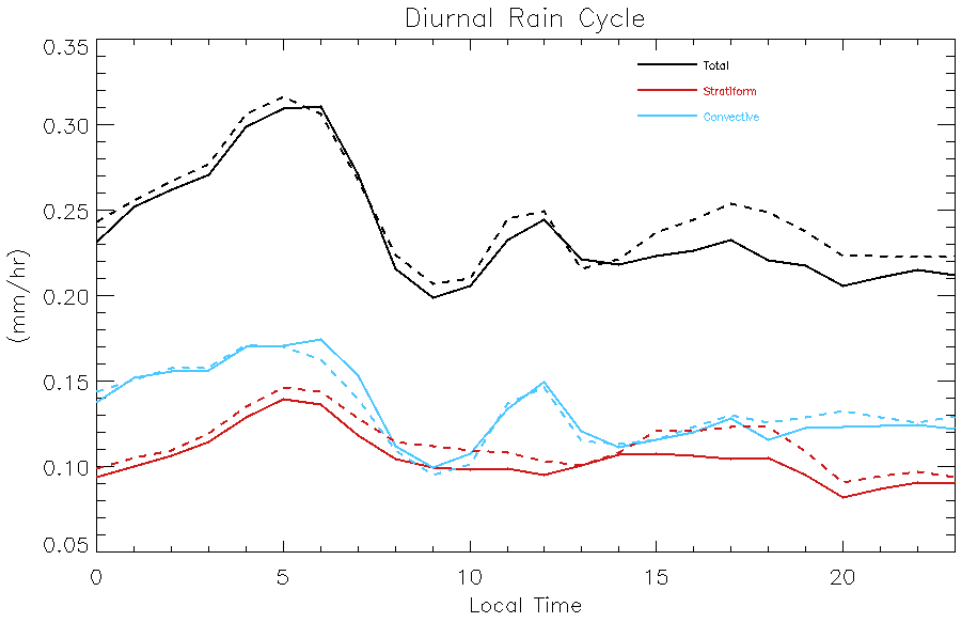

Figure 5.8: Diurnal rain cycle for stratiform (red), convective (blue), and total (black) rain as seen by SMART-R. The solid line represents full data set while the dashed line represents truncated data set.

that resulted in a late afternoon maximum in rainfall similar to what is found over land regions. However, both of these possible causes for the 1100-1300 LT maximum found in this study typically occur later in the day.

Studies using TRMM PR data to distinguish diurnal patterns in rainfall in the tropics don't correspond as well to the observations of the present study. Nesbitt and Zipser (2003) investigated three years of precipitation features throughout the global tropics and found a peak in rainfall over land from 1300-1900 LT, but very minimal diurnal variations over open ocean. Sobel et al. (2011) used TRMM PR data over islands in the Maritime Continent to try to detect a diurnal signal. They found that large islands (greater than 315 km^2) experience an increase in rain between roughly 0900-1500 LT, while small islands (less than 315 km^2) experience minimal diurnal signals. While they were only looking over land areas, compared to the majority

ocean area the present study is investigating, their results suggest that the shallow water regions of the lagoon might be important; i.e., the lagoon might experience enough afternoon solar heating that the entire atoll region acts as a 'large' island creating the heat island effect in the early afternoon. Oh et al. (2012) investigated the diurnal cycle in rainfall during the MJO over the western Maritime Continent and found a maximum in rainfall over oceanic areas around dawn, where as land regions experience a maximum during the late afternoon/early evening. The present study appears to combine results seen in these tropical studies. An early morning maximum is observed just as in the open ocean regions of the Oh et al. (2012) study, as well as the data from Jacobson (1976) and Gray and Jacobson (1977); this is in contrast to the other TRMM PR studies that don't reveal a dawn time maximum, or much of a diurnal cycle at all over ocean and small islands. On the other hand, the secondary maximum seen in the early afternoon appears similar to the maximum observed in the larger islands of the Sobel et al. (2011) study.

The absolute minimum for diurnal rain in the present study is found between 0800-1000 LT, sandwiched between the first and second peak; this minimum is only duplicated by Jacobson (1976) and Gray and Jacobson (1977). A slight evening minimum is found from 1800-2300 LT, but it is not as severe as the 0800-1000 LT minimum, nor is it as pronounced as the late evening minimum presented by Gray and Jacobson. Another way to look at the total time series is that from 0700–2300 LT, rain rates are 0.22 (mm/hr) $\pm$ 0.03 (mm/hr), which is fairly constant; the only strong diurnal signal is the sunrise maximum and other signals are minimal in comparison. This result is consistent with Yang and Slingo (2001), which found deepest convection to occur between 0200-0600 LT in the Indian Ocean; however, it disregards the secondary maximum that is visible in the convective rain signal from 1100-1300 LT, and slight peak in the stratiform rain signal from 1600-1800 LT.

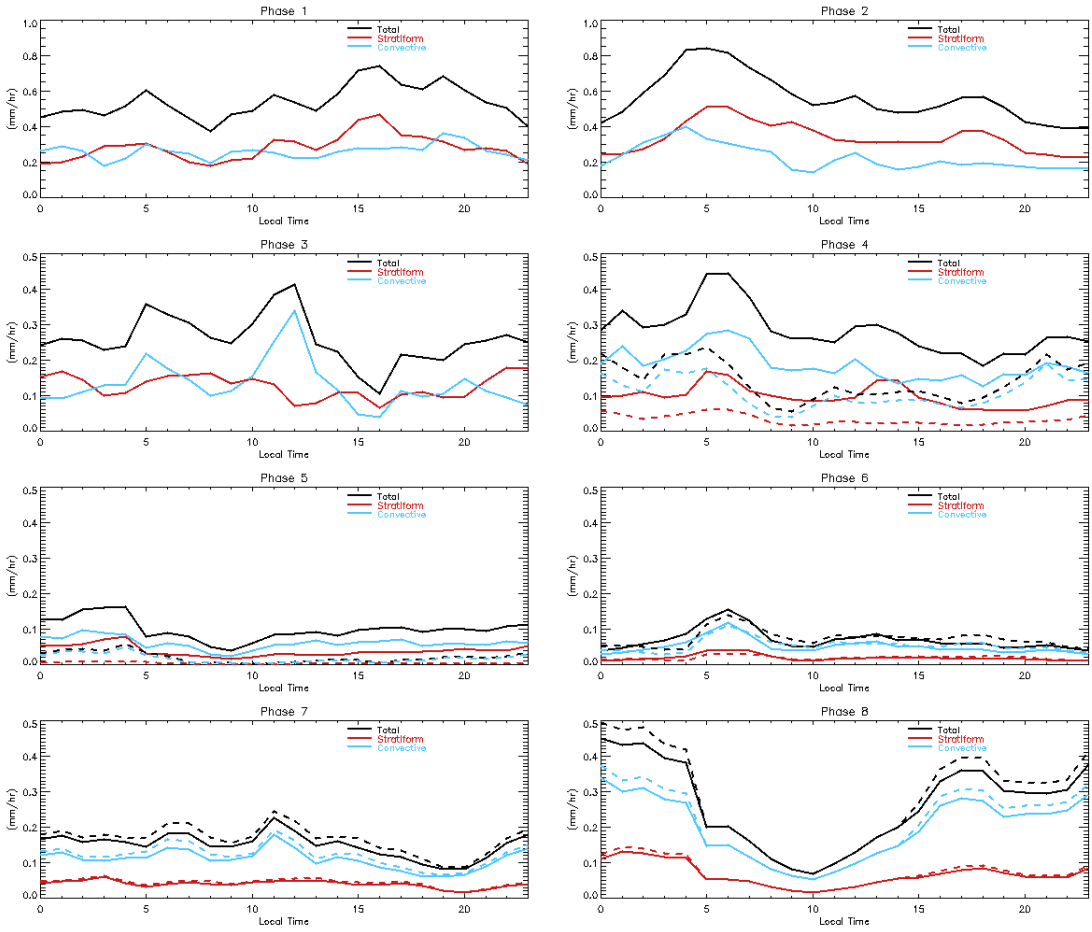

Figure 5.9: Diurnal cycle of rainfall by phase. Same as Figure 5.8 except separated by MJO phase. Note that phases 1 and 2 have different y-axis scales compared to the other phases.

This result also aligns with the TRMM PR studies mentioned above that showed minimal diurnal cycles over the ocean and small islands so long as the pre-dawn rainfall maximum is ignored.

Figure 5.9 shows the diurnal cycle of rain separated into MJO phase for both the full data set (solid lines) and truncated data set (dashed lines). For phases 1, 2, and 3 the data sets are identical and thus only one line is shown. Few of the diurnal phase lines follow the full campaign lines of Figure 5.8 except for stratiform rain in phase 2, convective rain in phase 3, and the full data set stratiform rain in phase 4.

During phase 1, an afternoon maximum between 1400 and 1700 LT is associated with an increase in stratiform rain, although slight maxima at 0500 and 1900 LT can be linked to increases in convective rain. A diurnal variation is much more obvious in phase 2 with a maximum occurring from 0300-0700 associated first with a buildup of convective rain and then being taken over by stratiform rain at 0500 LT. This rainfall time series is a classic example of mesoscale convective system evolution (e.g., Churchill and Houze 1984) and contributes significantly to the diurnal maximum seen in Figure 5.8. Smaller peaks occur at 1200 and 1700 LT due to convective and stratiform contributions, respectively.

Phase 3 diurnal variations are most closely associated with variations in convective rain. A small convective maximum at 0500 LT is followed by a larger maximum at 1200 LT, presumably from daytime heating. This second maximum appears to contribute significantly to the midday maximum seen in Figure 5.8. Stratiform rain is much more uniform throughout the day with a slight lull between 1100-2000 LT.

Phase 4 experiences the largest difference between the full and truncated data sets. Most of the stratiform diurnal signal is removed in the truncated data set, and the convective signal is lessened. Nevertheless, a general overnight maximum associated with increased convective rain is observed between 2000 and 0600 LT with lesser amounts during daylight. Phases 5 and 6 experience rather small rain amounts in the truncated data set, with the only significant diurnal feature being a slight increase in convective rain during 0500-0700 LT in phase 6. Phase 7, while also seeing very little diurnal variation in stratiform rain, experiences a diurnal variation in convective rain that most closely mirrors the large island from Gray and Jacobson (1977), i.e., the small peak from 0600-0800 LT, the larger peak around 1100 LT, and the minimum from 1700-2000 LT. While this result may be more coincidence than physical connection, it is prudent to point out that the generally sunny skies over

Addu Atoll during phase 7 might increase the heat island effect, though the lack of this structure in any other non-active phase would seem to diminish the validity of this argument.

Phase 8 perhaps shows the most interesting diurnal variation, which is fundamentally unchanged by the exclusion of days in the truncated data set. Largely driven by convective rain, the day can be split into two periods, a maximum from 1600-0500 LT and a minimum from 0500-1600 LT. This is unlike any other diurnal pattern observed during the DYNAMO campaign or in previous studies of tropical rainfall. A gradual buildup of convective rain begins at 1000 LT that reaches the maximum period at 1600 LT. A sharp drop is then observed from 0400-0500 LT. While the early morning maximum is in agreement with previous studies, the steady increase of rain beginning at 1000 LT that is sustained through the late afternoon and night appears to be an outlier. This is not only the most extreme diurnal cycle encountered in any of the phases, but also perhaps the most puzzling as a strict daytime/nighttime diurnal rain cycle doesn't seem to occur in any other tropical studies.

5.6 Humidity vs. Echo-top Heights

In order to better understand the relationship between environmental and convective properties in the initiation of the MJO, humidity retrievals from soundings are compared to SMART-R's echo-top height statistics (as described in Sec. 4.3.4), which serve as a proxy for the vertical extent of convective clouds. Figure 5.10 shows relative humidity as a function of height from soundings at Gan in colored contours and 10-dBz convective echo-top height counts from SMART-R in black contours for October 2011 - February 2012. The October MJO event had a gradual buildup in precipitation towards the end of phase 7, through phase 8, and into active phase 1

(Figure 5.1a). Two key features of Figure 5.10a are that during phase 8 when MJO initiation is beginning, an increase in echo tops in the mid- and upper troposphere appears to lead the moistening of the mid troposphere. October 10th for instance has a 30-count contour at 10 km, while relative humidity is less than 20% around 7 km. Secondly, a gradual increase in height of the 50-count contour line, as well as the 1-count contour line, is evident as phase 8 shifts into phases 1 and 2. For example, the average height of the 50-count contour line is approximately 7 km on October 10th, increasing to around 10 km on October 18th. This is perhaps akin to shallow and mid-level convection developing into deeper convection as described by Johnson et al. (1999) and Yoneyama et al. (2008). Both of these echo-top contour lines appear to lead humidity at these heights, i.e., regions inside of the 1-count contour fill with color as time goes on, and more green shows up inside the 50-count contours as time goes on (with the exception of October 18th). Both the Johnson et al. and Yoneyama et al. studies suggest detrainment of shallow clouds leads to moistening of the environment and deep convection. It appears that in the October case, low- and mid-level cloud growth leads relative humidity growth, which eventually develops into deep convection.

The November MJO case is more difficult to evaluate as the rain peak in phase 7 and the four-to-seven day rain pattern (Figure 5.1b) presents a more sporadic time series compared to the October event. Nonetheless, some telling details are observed in Figure 5.10b, which shows relative humidity and 10-dBz convective echo-top counts for November. First, a gradual increase of height in the 50-count contour line through phases 7 to 1 is observed just as in October. Rain events during phases 8 and 1 (November 15-18) and phase 2 (November 20-24) also follow a very similar pattern to the MJO rain events in October, i.e., convective clouds tend to lead relative humidity. The phase 8 to 1 period in particular has 30 and 50-count echo-

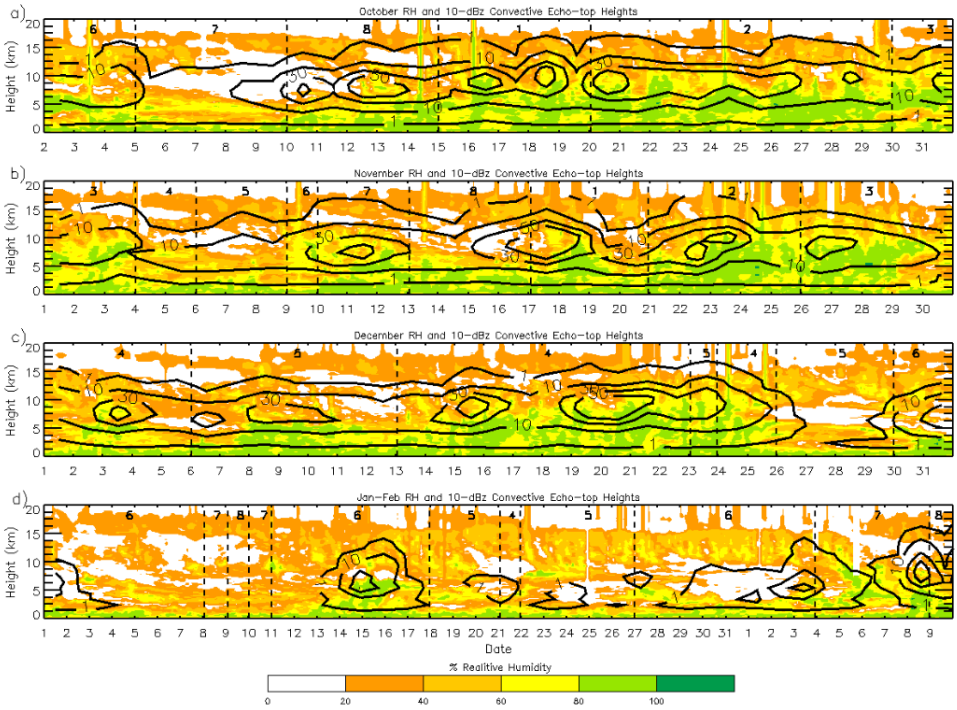

Figure 5.10: Humidity and 10-dBz convective echo-top heights. Humidity data from Gan soundings indicated by colored contours plotted along with 10-dBz convective echo-top heights for a) October, b) November, c) December, and d) January-February. Vertical dashed lines indicate MJO phases based on the Wheeler and Hendon index.

top height contours where the relative humidity is below 20%. The rain event and concurrent increase in convective echo top counts during phase 7, however, appear after the deepening of the moist layer. This is perhaps evidence of a fundamental difference of how the environment develops during active and suppressed phases of the MJO. Sobel et al. (2004) compare relative humidity and rain rates during the Kwajalein Experiment (KWAJEX) and through lag correlations suggest that lower troposphere relative humidity leads to the development of deep convection, which then moistens the upper troposphere. As KWAJEX was not an MJO related study, no comparison was made to whether the relationship could change depending on MJO phase. While it is out of the scope of this thesis, finding the lag correlation

between relative humidity and echo tops and relative humidity and rainfall using SMART-R could garner more definitive answers concerning the relationship between convection and atmospheric moisture.

Figure 5.10c shows relative humidity and 10-dBz convective echo tops for December, a time when the MJO was never in an active phase over the radar domain and when large rain amounts occurred during suppressed MJO phases. For all rain events during the month of December excluding the one at the end of the month, an increase in relative humidity appears to lead convective cloud development. This further suggests that there is a fundamental difference in the initiation of an MJO event compared to rain events occurring during suppressed phases.

January/February relative humidity and 10-dBz convective echo tops are shown in figure 5.10d. Convection is limited for a large majority of the month as expected by the lack of rainfall (figure 5.1d). February 8th is the only instance of 50-count echo tops during this time period, and unlike the initiation stages of the MJO, humidity appears to lead echo-top development. However, the moistening of the troposphere is most likely a result of the rain event on February 3rd, in which convective cloud development appeared to lead humidity. This goes against the argument made above that humidity leads convection during inactive phases, and vice versa during active phases, suggesting that a clear connection between which one leads and what the current MJO phase is not clear cut. However, based on the results from October-December that indicate some connection, this should be investigated further in future studies.

A caveat with any of the findings of this section is that while the echo-top data encompasses a wide area (the annulus between 20 and 146 km in the 180 degree sector that SMART-R sees), the soundings from Gan are at a single point located outside the area of the annulus, and most likely do not always accurately represent

the vertical humidity structure of the entire radar domain.

5.7 Wind Shear and Anvil

A major feature of the MJO is the overturning zonal circulations which consist of anomalously strong westerlies in the lower troposphere to the west of the 'active' region, and anomalously strong easterlies to the east (Figure 2.1); the winds are reversed at upper levels (Madden and Julian, 1972; Zhang, 2005). Figure 5.11 shows zonal winds from the soundings at Gan in the colored contours, with reds indicating westerlies and blues indicating easterlies; 10-dBz anvil/clutter echo-top heights are plotted in yellow. With the exception of data before October 28th, it can be assumed that any echo tops above 3 km are anvil because the SQI filter removes clutter aloft.

The general wind structure observed in Figure 5.11 is three layers, i.e., westerlies occurred in the lower troposphere, easterlies in the middle and upper troposphere, and westerlies above the tropopause (at approximately 15 km). The thickness of the layers did vary however. Wind shear throughout the entire column appears to be minimal during initiation and the first part of the active phase as indicated by the blues and reds that are lighter in shade during this time. Low-level easterlies also only appear during phases 8 and 1, with the exception of early January (the MJO was considered 'weak' during this time). This is generally an expected observation as the only time low-level easterlies should occur would be when the MJO convective center is located to the west, which occurs during the end of phase 8, into phases 1 and 2.

Anvil counts can be seen to increase towards the end of phase 2 and into phase 3 for both the October and November MJO cases. As upper level easterlies increase during this time period (signified by the darker shades of blue around 15 km) and

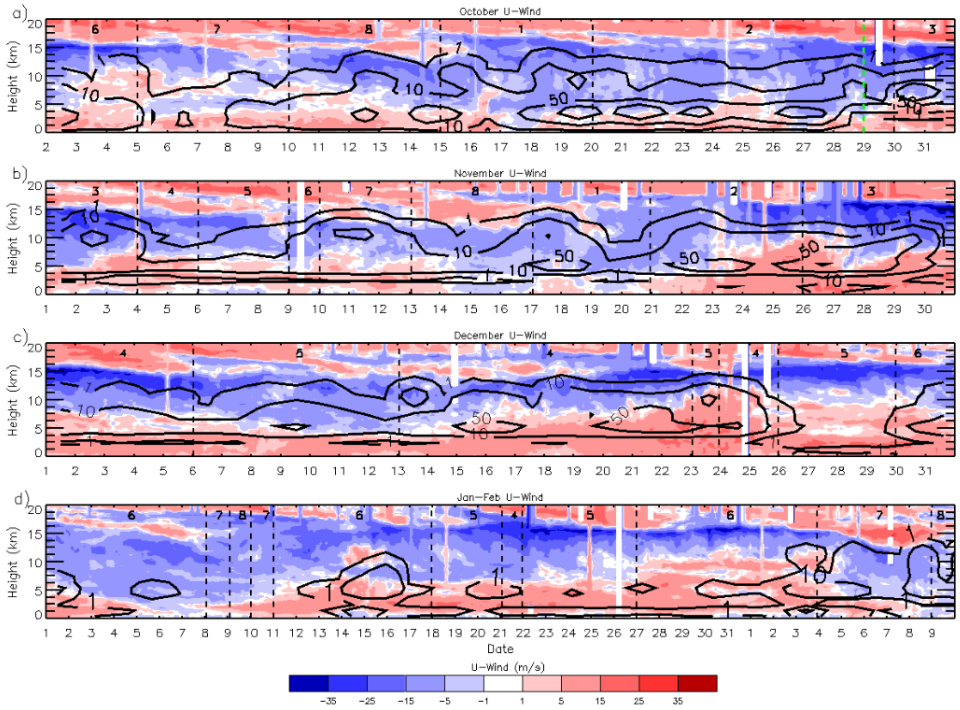

Figure 5.11: Zonal winds and 10-dBz anvil/clutter echo-top heights. Zonal winds from Gan soundings (blue indicates westerlies, red indicated easterlies) plotted with 10-dBz anvil/clutter echo tops in yellow contours for a) October, b) November, c) December, and d) January-February. Vertical dashed black lines indicate MJO phases based on the Wheeler and Hendon index. The green dashed line indicates when SQI data began to be saved.

lower level westerlies increase (signified by darker reds in the lower troposphere), a clear increase in anvil (defined as pixels that have no echo at 3 km, or are below the weak echo threshold as described in Sec. 4.3.3) is observed. During these periods, it is likely that the stronger shear enhanced detrainment from the deep convective system to produce more anvil. Figure 10d shows January, a very dry period of time that saw minimal cloud development. Because deep convection was minimal, the increased shear that develops beginning around January 20th does not correspond to increased anvil, let alone any anvil at all.

Anvil can also increase due to wind shear variations associated with individual

events. A good example of this is on 17 - 18 November in Figure 5.11b. During this time, low-level winds shift from easterlies to westerlies, while at the same time a 'pocket' of easterlies appears to over-take westerlies around 12 km. This abrupt switch in wind direction both near the surface, and aloft should in theory result in shearing of clouds, which is exactly what is observed with a 50-count anvil contour recorded. Another instance of increased shear occurs around 27 November. Some of the strongest westerlies of the campaign at the surface were recorded then; easterlies above 15 km are also detected, another uncommon feature. This is actually due to Tropical Storm 05A (name as given by the Joint Typhoon Warming Center), which was situated to the north of Gan and moved towards the north and west.

Stratiform rain echo tops (not shown) also appear to have an interesting relationship with the wind structure. The low-level easterlies that appear in phases 8 and 1 correspond to an immediate dissipation in stratiform echo counts, followed by rapid enhancement once easterlies weaken. This is similar to the findings of Kiladis et al. (2005) which showed enhanced stratiform production following the westerly wind burst.

It is necessary to point out that the material presented in this section is a preliminary analysis of a much richer topic. Shear was unexpected and may have implications for the organization and evolution of mesoscale systems associated with the MJO. This is certainly an area that deserves attention for future work with this data set.

6. DISCUSSION

Besides producing a high-quality radar data set and presenting a census of SMART-R observations collected during the DYNAMO/CINDY2011 campaign, a goal of this thesis was to try to identify radar-observed features of the MJO that can lead to a more localized MJO phase index. While the methods of Wheeler and Hendon (2004) and other MJO indices are based on global analyses of model and passive satellite data, the information gathered from ground-based precipitation radars, or even the TRMM PR, might reveal better information about the MJO over a smaller area.

Although this study only had two MJO events during its nineteen-week campaign, valuable information was still collected. As seen in Figure 5.1, daily stratiform rain amounts only exceed convective rain in phases 1, 2, and 3 (with the exception of December 9th which occurred during the time period where an unusually strong Kelvin wave was observed). While convective rain can exceed stratiform rain during active phases, a condition of being in the suppressed phase can be larger convective rain amounts than stratiform rain, i.e., if the daily rain amount of convective rain exceeds that of stratiform rain, the MJO is suppressed in the radar domain. This is also shown in figure 6 as stratiform rain only exceeds convective rain in phases 1 and 2.

Regarding fractional area of rain by precipitation type (Figure 5.2), no discernible relation *between* convective and stratiform rain area can determine phase; convective area remains fairly constant regardless of phase. As mentioned before however, stratiform area percentages increase significantly during active phases of the MJO. Again disregarding December data, anytime stratiform rain exceeded 20% radar coverage, the MJO was either initiating or fully developed. This ambiguity in using area

percentage to determine the initiation of the MJO is evident by the contrast in the October and November MJO events. While the October event had a gradual buildup, the 5-day episodic large rain days of the November MJO makes pinpointing the time of initiation difficult. One could argue that the rain peak during phase 7 is sufficient proof of MJO initiation, although its peak is dwarfed by the two successive peaks during phases 1 and 2, and thus could be an isolated event. Regardless, rain percentage area, while providing some useful information for determining initiation, cannot be used alone as the deciding factor whether initiation is occurring.

Echo-top heights can also be considered in determining the initiation of the MJO, but the different patterns of the two MJO events followed by the unorthodox weather of December makes this determination difficult. Of note though is a period of relatively low counts (equivalent to low overall rain coverage) during phase 7 in October and phase 5 and 6 in November. With phase 8 in October and phase 7 in November, comes a significant increase in 10- and 40-dBz echotops; just as in the rain area discussed above. This definition is dependent on classifying phase 7 in November as initiation and not as a random rain event.

The number of echo-top counts, particularly at a 10-dBz threshold, appears to provide evidence that the MJO is active. Again, disregarding the December rain event (particularly around 20 - 23 December), once 10-dBz echo-top counts exceed 350 (signified in yellow in Figure 5.3) at any height level, the MJO is in the active phase. While the MJO can be in the active phase and not reach this count number, if counts exceed a value of 350 (or even 300) which indicates fairly enhanced cloud coverage, the MJO is almost certainly in the active phase. A difficulty with this approach however is knowing to disregard the December data based solely from ground observations.

The diurnal cycle of rainfall may in fact provide the best indicator of MJO ini-

tiation of any of the radar statistics discussed in this thesis. As seen in Figure 5.9, during phases 5, 6 and 7, when the MJO should be 'suppressed' over Gan, very little diurnal cycle is apparent. As discussed in section 5.5, a slight peak in convection is apparent during phase 6 around dawn, and phase 7 also experiences a slight diurnal pattern in the convective signal. Phase 8 however has such a different diurnal signal (heavy nighttime rain with minimal daytime rain), that any days with rainfall patterns similar to it might indicate that the MJO is beginning to initiate, or preparing to transition to phase 1 where initiation will occur. An issue with this approach is sample size. Phase 8 only occurred on 11 days of the campaign, and perhaps this diurnal signal would diminish with more data. In fact with only two legitimate MJO events during the 131 day campaign, it is difficult to make any firm judgments about MJO initiation based on the limited data set. More data, possibly from TRMM PR, is needed to confirm the statistical findings of this study, with the exception of the obvious results that it rains more during active phases and stratiform rain exceeds convective rain during the active phases.

Sounding data, in conjunction with radar data, may provide more useful information for determining a localized index. As discussed in section 5.6, there appears to be a connection between humidity throughout the vertical column and echo top counts, which might provide clues on when MJO initiation is occurring. Again however, more data over additional MJO events would need to be evaluated to discern between actual characteristics of the MJO and random events. Wind data from soundings could also be used to determine MJO initiation as the zonal wind structure appears to vary significantly during the active and suppressed MJO phases. The brief period of low-level westerlies right before an MJO event in Gan could signify initiation.

The development of a localized MJO index is within reach, but more data and

observations are needed before anything definitive can be developed. The logistical difficulties in having a sounding network and ground-based radar network are a difficult hurdle to overcome, and reliance on systems such as TRMM is probably the most logical step in further developing a localized MJO index. Using smaller windows in reanalyses and OLR data in indices such as the one described by Wheeler and Hendon (2004) can also be experimented with, but difficulties may arise from scaling these products down to the size of a typical radar domain. In the mean time, the current methods of Wheeler and Hendon (2004) and others will remain the standard in describing the progression and state of the MJO and continued efforts should go into improving those indices, most importantly the difficulties that arise from passing atmospheric Rossby and Kelvin waves.

7. CONCLUSION

The purpose of this thesis was to describe the methods used to collect and convert raw SMART-R full-volume scan data from the DYNAMO/CINDY2011 campaign into quality-controlled reflectivity data files that could be used for analysis by the wider community, and then provide a census of rain statistics derived from the quality-controlled files that include rainrates, echo-top heights, and convective/stratiform separations, including a modified convective/stratiform separation. Every ten minutes, two volume scans were created, merged, and run through quality control algorithms that included a calibration correction of -8 dB, an attenuation correction, and a correction for an apparent tilt of 0.75 degrees towards azimuth 285 degrees. The polar data was then converted into Cartesian coordinates, and a final SQI correction was performed to remove second-trip echo. For data collected on 2 October - 27 October, SQI data was unavailable and the resulting quality controlled files contain some amount of second trip echo. In addition, some anomalous propagation occasionally occurs (mostly in January) which outlines the atoll to the north of Addu. This is an issue to look into during future processing jobs of this data set, however, any anomalous propagation from the atoll is negligible to the radar statistics presented in this thesis.

The quality-controlled reflectivity files were then run through algorithms that determined rainrates, echo-top heights at 10-, 20-, 30-, and 40-dBz thresholds, and a convective/stratiform separation. It was determined through visible inspection of the convective/stratiform separation maps that the CS algorithm was inadequate in resolving the correct classification for shallow, isolated rain. The 3DCS algorithm was developed, which used the output of the CS algorithm, 10-dBz echo-top height

data, and an isolation parameter that requires pixels that are reclassified to not be within 10 km of other echo. This resulted in a much more realistic classification, enhancing the amount of shallow convection, although the algorithm still has room for improvement, specifically the use of the isolation parameter. The choice of 10 km for the isolation parameter could cause some actual shallow convection to be labeled as stratiform simply because of its proximity to other echo.

Rain statistics were presented for the campaign based on the algorithms described above. Two MJO events were captured during this study (October and November), as well as an unusual rainy 'suppressed' phase in December caused most likely by strong convectively coupled atmospheric waves, and a very dry 'suppressed' phase in January where the MJO index was considerably weak. While worthwhile observations were taken, the stark differences in the two MJO events' rainfall patterns make it difficult to draw significant conclusions on exact characteristics of the MJO except other than each event can behave differently. More analysis is needed to determine which MJO event during this campaign most resembles the 'normal' MJO event, or if both patterns are common.

The evolution of echo-top heights also can reveal characteristics of the MJO, however, just as with the rain statistics, the small sample size of this campaign makes it exceedingly difficult to pinpoint behavior that is typical of all MJO events. Some connection between humidity and echo top heights appears to exist (that humidity follows echo top development during MJO initiation and vice versa during inactive phases), but more observations are necessary to validate this finding. The role of shear in the initiation and evolution of the MJO also needs to be examined further. While decreased shear appeared to accompany MJO initiation, the amount of shear observed throughout the entire campaign was unexpected.

This thesis describes a census of the data collected by SMART-R, however, much

more is still to be done. The data collected from SMART-R can be used for many other applications including but not limited to a latent heating analysis and the effects on precipitation with passing atmospheric waves. In addition, there is an entire RHI data set from SMART-R that needs to be processed and examined. Despite blockage over half of SMART-R's intended domain, as well as a seven-week premature end to the campaign, SMART-R has provided the scientific community with an invaluable data set that can assist in better understanding the Madden-Julian Oscillation both on its own, and in conjunction with observations taken by other instruments.

REFERENCES

Biggerstaff, M. I., L. J. Wicker, J. Guynes, and Coauthors, 2005: The Shared Mobile Atmospheric Research and Teaching Radar: A Collaboration to Enhance Research and Teaching. *Bulletin of the American Meteorological Society*, 1263–1274.

Churchill, D. D. and R. A. Houze, Jr., 1984: Development and Structure of Winter Monsoon Cloud Clusters on 10 December 1978. *Journal of the Atmospheric Sciences*, **41**, 933–960.

DeMott, C. A. and S. A. Rutledge, 1998: The Vertical Structure of TOGA COARE Convection. Part I: Radar Echo Distributions. *Journal of the Atmospheric Sciences*, **55**, 2730–2747.

DYNAMO, 2011: DYNAMO Operations Plan. Tech. rep., NSF. URL `http://www.eol.ucar.edu/projects/dynamo/documents/index.html`.

Frederick, K. and C. Schumacher, 2008: Anvil Characteristics as Seen by C-POL during the Tropical Warm Pool International Cloud Experiment (TWP-ICE). *Monthly Weather Review*, **136**, 206–222.

Google, 2012: Addu atoll map. URL `google.maps.com`.

Gottschalck, J., V. Kousky, W. Higgins, and M. L'Heureux, 2005: Madden Julian Oscillation MJO Summary. Tech. rep., NOAA. URL `http://www.cpc.ncep.noaa.gov/products/precip/CWlink/MJO/mjo.shtml`.

Gray, W. M. and R. W. Jacobson, 1977: Diurnal Variations of Deep Cumulus Convection. *Monthly Weather Review*, **105**, 1171–1188.

Hendon, H. H., C. Zhang, and J. D. Glick, 1999: Interannual Variation of the Madden-Julian Oscillation during Austral Summer. *Journal of Climate*, **12**, 2538–2550.

Houze, R. A., Jr., 1997: Stratiform Precipitation in Regions of Convection: A Meteorological Paradox? *Bulletin of the American Meteorological Society*, 2179–2196.

Houze, R. A., Jr., S. Brodzik, C. Schumacher, S. E. Yuter, and C. R. Williams, 2004: Uncertainties in Oceanic Radar Rain Maps at Kwajalein and Implications for Satellite Validation. *Journal of Applied Meteorology*, **43**, 1114–1132.

Jacobson, R. W., 1976: Diurnal Variation of Oceanic Deep Cumulus Convection: Observational Evidence. M.S. thesis, Colorado State University. Fort Collins, CO.

Johnson, R. H., P. E. Ciesielski, and J. A. Cotturone, 2001: Multiscale Variability of the Atmospheric Mixed Layer over the Western Pacific Warm Pool. *Journal of the Atmospheric Sciences*, **58**, 2729–2750.

Johnson, R. H., T. M. Rickenbach, S. A. Rutledge, P. E. Ciesielski, and W. H. Schubert, 1999: Trimodal Characteristics of Tropical Convection. *Journal of Climate*, **12**, 2397–2418.

Kiladis, G. N., K. H. Straub, and P. T. Haertel, 2005: Zonal and Vertical Structure of the Madden-Julian Oscillation. *Journal of the Atmospheric Sciences*, **62**, 2790–2809.

Knutson, T. R. and K. M. Weickmann, 1987: 30-60 day Atmospheric Oscillations: Composite Life Cycles of Convection and Circulation Anomalies. *Monthly Weather Review*, **115**, 1407–1436.

Knutson, T. R., K. M. Weickmann, and J. E. Kutzbach, 1986: Global-Scale Intraseasonal Oscillations of Outgoing Longwave Radiation and 250 mb Zonal Wind during Northern Hemisphere Summer. *Monthly Weather Review*, **114**, 605–623.

Lau, K.-M. and P. H. Chan, 1985: Aspects of the 40-50 Day Oscillation during the Northern Winter as Inferred from Outgoing Longwave Radiation. *Monthly Weather Review*, **113**, 1889–1909.

Lau, K.-M. and H.-T. Wu, 2010: Characteristics of Precipitation, Cloud, and Latent Heating Associated with the Madden-Julian Oscillation. *Journal of Climate*, **23**, 504–518.

Lerach, D. G., S. A. Rutledge, C. R. Williams, and R. Cifelli, 2010: Vertical Structure of Convective Systems during NAME 2004. *Monthly Weather Review*, **138**, 1695–1714.

Lin, J., B. Mapes, M. Zhang, and M. Newman, 2004: Stratiform Precipitation, Vertical Heating Profiles, and the Madden-Julian Oscillation. *Journal of the Atmospheric Sciences*, **61**, 296–309.

Lo, F. and H. H. Hendon, 2000: Emperical Extended-Range Prediction of the Madden-Julian Oscillation. *Monthly Weather Review*, **128**, 2528–2543.

Madden, R. A., 1986: Seasonal Variations of the 40-50 Day Oscillation in the Tropics. *Journal of the Atmospheric Sciences*, **43 (24)**, 3138–3158.

Madden, R. A. and P. R. Julian, 1971: Detection of a 40-50 Day Oscillation in the Zonal Wind in the Tropical Pacific. *Journal of the Atmospheric Sciences*, **28**, 702–708.

Madden, R. A. and P. R. Julian, 1972: Decription of Global-Scale Circulation Cells in the Tropics with a 40-50 Day Period. *Journal of the Atmospheric Sciences*, **29**, 1109–1123.

Matthews, A. J., 2000: Propagation mechanisms for the Madden-Julian Oscillation. *Quarterly Journal of the Royal Meteorological Society*, **126 (569)**, 2637–2651.

Nesbitt, S. W. and E. J. Zipser, 2003: The Diurnal Cycle of Rainfall and Convective Intensity according to Three Years of TRMM Measurements. *Journal of Climate*, **16**, 1456–1475.

Oh, J.-H., K.-Y. Kim, and G.-H. Lim, 2012: Impact of MJO on the diurnal cycle of rainfall over the western Maritime Continent in the austral summer. *Climate Dynamics*, **38**, 1167–1180.

Rinehart, R. E., 2010: *Radar For Meteorologists*. 5th ed., Rinehart Publications, Nevada, MO.

Schumacher, C. and R. A. Houze, Jr., 2000: Comparison of Radar Data from the TRMM Satellite and Kwajalein Oceanic Validation Site. *Journal of Applied Meteorology*, **39**, 2151–2164.

Schumacher, C. and R. A. Houze, Jr., 2003: The TRMM Precipitation Radar's View of Shallow, Isolated Rain. *Journal of Applied Meteorology*, **42**, 1519–1524.

Schumacher, C. and R. A. Houze, Jr., 2006: Stratiform precipitation production over sub-Saharan Africa and the tropical East Atlantic as observed by TRMM. *Quarterly Journal of the Royal Meteorological Society*, **132**, 2235–2255.

Slingo, J., D. Rowell, K. R. Sperber, and F. Nortley, 1999: On the predictability of

the interannual behaviour of the Madden-Julian Oscillation and its relationshp to El Nino. *Quarterly Journal of the Royal Meteorological Society*, **125**, 853–609.

Sobel, A. H., C. Burleyson, and S. Yuter, 2011: Rain on small tropical islands. *Journal of Geophysical*, **116**.

Sobel, A. H., S. E. Yuter, C. S. Bretherton, and G. N. Kiladis, 2004: Large-Scale Meteorology and Deep Convection during TRMM KWAJEX. *Monthly Weather Review*, **132**, 422–444.

Steiner, M., R. A. Houze, Jr., and S. E. Yuter, 1995: Climatological Characterization of Three-Dimensional Storm Structure from Operational Radar and Rain Gauge Data. *Journal of Applied Meteorology*, **34**, 1978–2007.

Wheeler, M. C. and H. H. Hendon, 2004: An All-Season Real-Time Multivariate MJO Index: Development of an Index for Monitoring and Prediction. *Monthly Weather Review*, **132**, 1917–1932.

Yang, G.-Y. and J. Slingo, 2001: The Diurnal Cycle in the Tropics. *Monthly Weather Review*, **129**, 784–801.

Yoneyama, K., Y. Masumoto, and Coauthors, 2008: MISMO FIELD EXPERIMENT IN THE EQUATORIAL INDIAN OCEAN. *Bulletin of the American Meteorological Society*, 1889–1903.

Yuter, S. E. and R. A. Houze, Jr., 1998: The natural variability of precipitating clouds over the western Pacific warm pool. *Quarterly Journal of the Royal Meteorological Society*, **124**, 53–99.

Zhang, C., 2005: Madden-Julian Oscillation. *Reviews of Geophysics*, **43**, 1–36.

Zhang, C. and M. Dong, 2004: Seasonality of the Madden-Julian oscillation. *Journal of Climate*, **17**, 3169–3180.

APPENDIX A

MONTHLY ECHO-TOP FIGURES

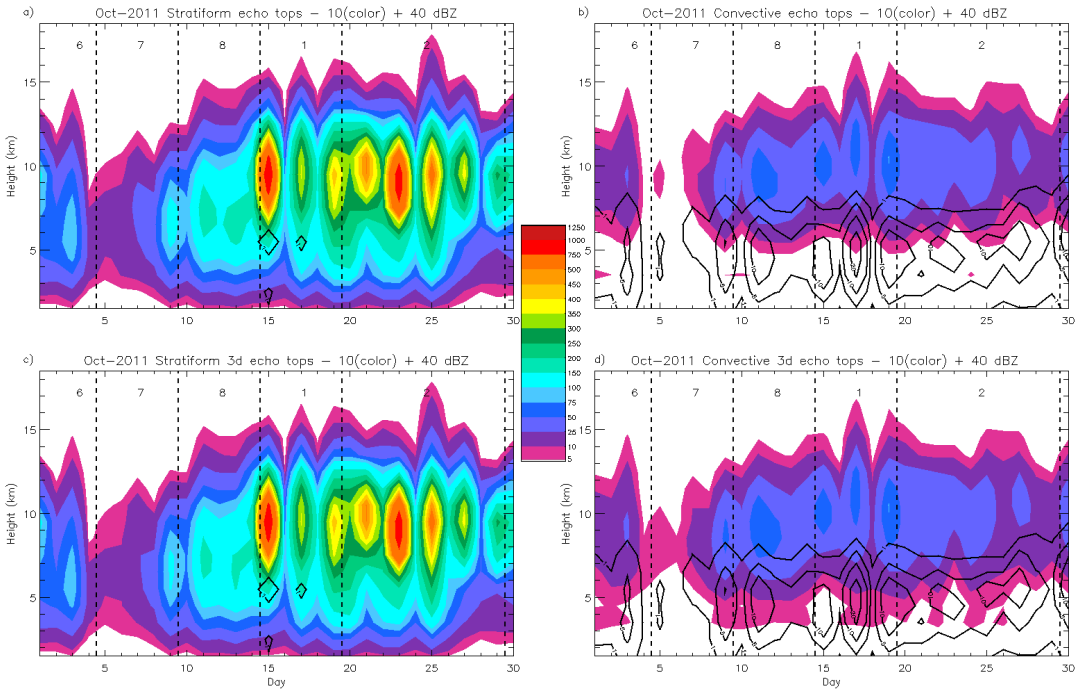

Figure A.1: October echo tops. Same as Figure 5.4 except for October.

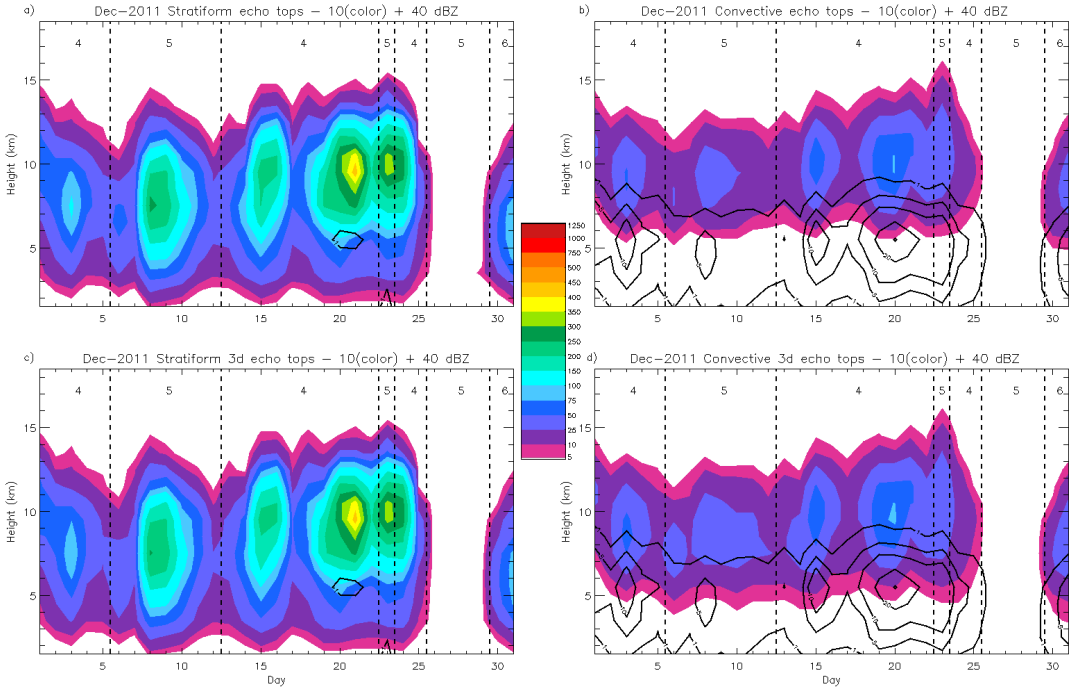

Figure A.2: December echo tops. Same as Figure 5.4 except for December.

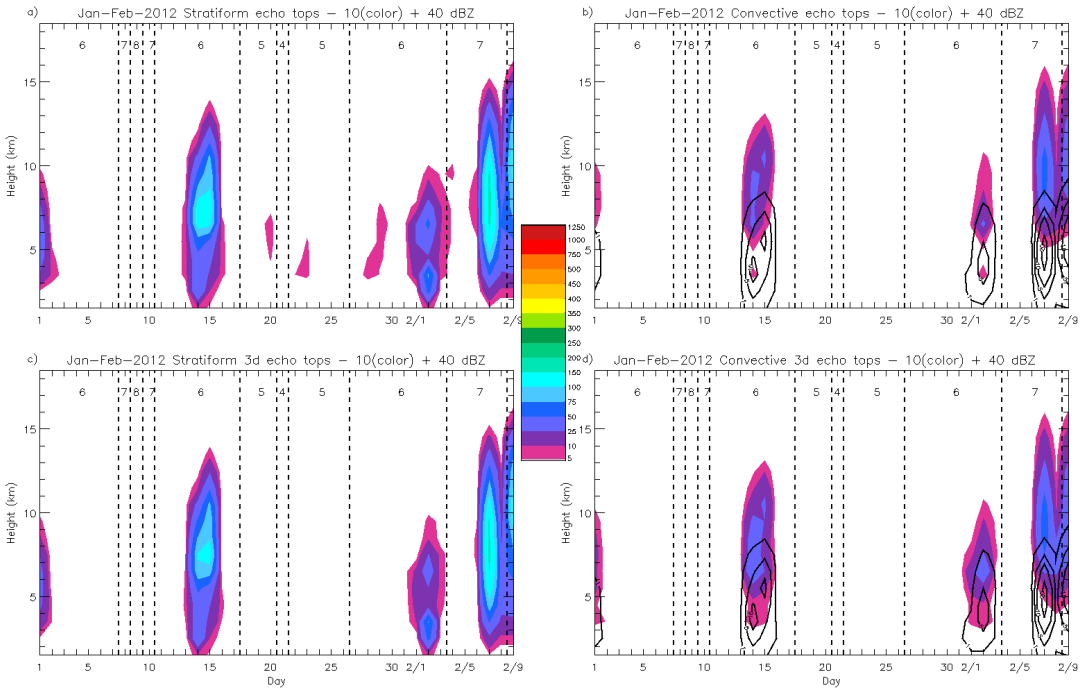

Figure A.3: January-February echo tops. Same as Figure 5.4 except for January-February.